

Intrinsic mass-richness relation of clusters from THE THREE HUNDRED hydrodynamic simulations

MINGJING CHEN,^{1,2} WEIGUANG CUI,^{3,4,5,*} WENJUAN FANG,^{1,2} AND ZHONGLUE WEN^{6,7}

¹*CAS Key Laboratory for Research in Galaxies and Cosmology, Department of Astronomy, University of Science and Technology of China, Hefei, Anhui, 230026, People's Republic of China*

²*School of Astronomy and Space Science, University of Science and Technology of China, Hefei, Anhui, 230026, People's Republic of China*

³*Departamento de Física Teórica, Universidad Autónoma de Madrid, Módulo 15, E-28049 Madrid, Spain*

⁴*Centro de Investigación Avanzada en Física Fundamental (CIAFF), Facultad de Ciencias, Universidad Autónoma de Madrid, 28049 Madrid, Spain*

⁵*Institute for Astronomy, University of Edinburgh, Royal Observatory, Edinburgh EH9 3HJ, UK*

⁶*CAS Key Laboratory of FAST, NAOC, Chinese Academy of Sciences, Beijing 100101, People's Republic of China*

⁷*National Astronomical Observatories, Chinese Academy of Sciences, 20A Datun Road, Chaoyang District, Beijing 100101, People's Republic of China*

(Dated: April 3, 2024; Received February 07, 2024; Accepted March 28, 2024)

Submitted to ApJ

ABSTRACT

The main systematics in cluster cosmology is the uncertainty in the mass-observable relation. In this paper, we focus on the most direct cluster observable in optical surveys, i.e. richness, and constrain the intrinsic mass-richness (MR) relation of clusters in THE THREE HUNDRED hydrodynamic simulations with two runs: GIZMO-SIMBA and GADGET-X. We find that modeling the richness at fixed halo mass with a skewed Gaussian distribution yields a simpler and smaller scatter compared to the commonly used log-normal distribution. Additionally, we observe that baryon models have a significant impact on the scatter, while exhibiting no influence on the mass dependence and a slight effect on the amplitude in the MR relation. We select member galaxies based on both stellar mass M_* and absolute magnitude \mathcal{M} . We demonstrate that the MR relation obtained from these two selections can be converted to each other by using the $M_* - \mathcal{M}$ relation. Finally, we provide a 7-parameter fitting result comprehensively capturing the dependence of the MR relation on both stellar mass cutoff and redshift.

Keywords: Galaxy cluster

1. INTRODUCTION

Galaxy clusters (hereafter clusters for simplicity), as the largest gravitationally bound structures in the Universe, hold significant importance in both cosmology and astrophysics (see Kravtsov & Borgani 2012; Allen et al. 2011; Wechsler & Tinker 2018, etc. for reviews). Accurate measurement of cluster mass is one of the most crucial steps for these studies (Pratt et al. 2019).

Different methods can be used to determine individual cluster's mass. The simplest and oldest method is dynamical analysis, using galaxy velocity dispersion with the assumption of dynamical equilibrium (Zwicky

mingjing@mail.ustc.edu.cn

weiguang.cui@uam.es

wjfang@ustc.edu.cn

zhonglue@nao.cas.cn

* Talento-CM fellow

1937; Li et al. 2021). X-ray observations estimate cluster mass through gas density and temperature profiles with the hydrostatic equilibrium assumption (see Ansarifard et al. 2020; Pearce et al. 2020; Gianfagna et al. 2021, for example). On top of that, the strong and weak lensing signals from shape distortions of background galaxies provide a most direct and powerful method to measure the cluster mass (e.g. Meneghetti et al. 2010; Okabe & Smith 2016). In general, these different methods yield consistent results in previous studies (e.g. Lewis et al. 1999).

However, these methods require high-quality or long-term spectral observations, restricting accurate measurements to only a small number of clusters. To overcome this limitation and to obtain a large number of cluster masses extending to high redshift which is important for cosmology, the cluster mass-observable relation is commonly employed, i.e. estimating the masses of a cluster sample using more easily accessible observables as mass proxies. This approach has been widely utilized in cosmological research after being calibrated with direct measures of cluster masses, such as weak lensing (e.g. McClintock et al. 2019), or through self-calibration when constraining cosmological parameters (e.g. Oguri & Takada 2011).

Different mass proxies are utilized in different surveys. In X-ray surveys, commonly used mass proxies include the gas mass, gas temperature, gas luminosity in different X-ray bands or integrated (e.g. Mulroy et al. 2019; Babyk & McNamara 2023). In Sunyaev-Zel'dovich (SZ) surveys, the projected integrated SZ flux is usually used (e.g. Planck Collaboration et al. 2016a). Optical surveys make use of observables such as richness, optical luminosity and galaxy overdensity (e.g. Pearson et al. 2015) as mass proxies. Compared to X-ray and SZ surveys, optical surveys have a larger field of view and can easily extend to higher redshift with bigger signal-to-noise ratios. Multi-wavelength bands in optical surveys are generally available which can provide photometric redshift if the spectroscopic redshift is not available. Albeit a slightly large error, this enables the detection of clusters to higher redshifts. Consequently, a large sample of clusters spanning a wide range of mass and redshift can be constructed (e.g. Wen et al. 2012; Rykoff et al. 2014; Wen & Han 2021). Among these optical observables, richness is the most direct one and exhibits a small scatter (Old et al. 2014, 2015; Pearson et al. 2015), which is of utmost importance for cosmological constraints. Although cluster member identification suffers from foreground and background contamination, as well as these interlopers (Wojtak et al. 2018), which introduce uncertainties in richness. Advancements in cluster finding

techniques have enabled richness to remain a reliable mass proxy with low scatter (Rykoff et al. 2012, 2014).

Numerous articles have been devoted to constraining the mass-richness relation, hereafter MR relation. For instance, some studies are based on X-ray measurements, such as Capasso et al. (2019) using the ROSAT All-Sky Survey and Chiu et al. (2023) using the extended ROentgen Survey with an Imaging Telescope Array (eROSITA), and some studies based on SZ measurements, like Saro et al. (2015) and Bleem et al. (2020), utilizing the South Pole Telescope (SPT). Additionally, studies from optical surveys, such as Murata et al. (2018) and Simet et al. (2017) using the Sloan Digital Sky Survey (SDSS) redMaPPer clusters, Murata et al. (2019) utilizing the Subaru Hyper Suprime-Cam (HSC), and Costanzi et al. (2021) employing the Dark Energy Survey (DES), are based on the weak lensing measurements of clusters.

These studies typically employ a power-law model to describe the MR relation. Most of them report consistent dependencies on mass, aligning with the predictions of self-similarity (Kaiser 1986). However, discrepancies arise when it comes to the redshift dependence. Andreon & Congdon (2014) and Saro et al. (2015) argue that the data is consistent with no redshift evolution within 1σ , while Capasso et al. (2019) demonstrates a strong negative evolution trend. Regarding the treatment of the richness probability distribution, most studies adopt a log-normal distribution, albeit employing different formulas for the scatter. Some studies (Murata et al. 2018, 2019) take it as a linear function of the logarithm of mass and redshift to account for observational effects. Others (Capasso et al. 2019; Bleem et al. 2020; Costanzi et al. 2021) model it as a Poisson term plus an intrinsic scatter term, separately accounting for projection effects.

Few articles investigate thoroughly the intrinsic MR relation from a theoretical standpoint. In this work, we aim at such a study. Specifically, we employ a power-law model for the MR relation, similar to previous studies, but delve deeper to examine its dependencies on redshift, limit of galaxy stellar mass or magnitude for member galaxy selection. The most important aspect of our work lies in the choice for the richness probability distribution. Instead of employing a simple log-normal distribution as in previous studies, we utilize a skewed Gaussian distribution with a scatter based on the Halo Occupation Distribution (HOD) model (Jiang & van den Bosch 2017). Notably, this choice results in a mass-independent intrinsic scatter. Our work is based on two different hydro-simulations starting from the same initial conditions but different baryon models (Cui et al. 2018, 2022). The outcomes of this study

can improve our understanding of the MR relation, and contribute to accurate modeling approaches, which, in turn, can hopefully reduce the scatter in the MR relation and ultimately tighten the constraints on cosmological parameters.

This paper is organized as follows. In Section 2, we introduce THE THREE HUNDRED on which our analysis is based. Section 3 describes our model for the MR relation with a skewed Gaussian distribution for the richness. In Section 4, we present the main results for both selection of galaxies based on galaxy stellar mass and on magnitude. Section 5 involves comparing our results with other prescriptions for the richness distribution, as well as including the dependences on the stellar mass limit and redshift. We also make comparison with other findings from the literature. Finally, we summarize and conclude in Section 6.

2. THE SIMULATED DATA

2.1. THE THREE HUNDRED

THE THREE HUNDRED (hereafter THE300) (Cui et al. 2018) performs hydrodynamic cosmological zoom-in re-simulations in 324 selected cluster regions. These regions are spherical with a radius of $15 h^{-1} \text{Mpc}$, centered around the 324 most massive clusters extracted from the MultiDark Planck 2 simulation (MDPL2) (Klypin et al. 2016). MDPL2 is a dark matter-only N-body simulation with a comoving length of $1 h^{-1} \text{Gpc}$, using 3840^3 dark matter particles of mass $m_{\text{DM}} = 1.5 \times 10^9 h^{-1} M_{\odot}$, and adopts cosmological parameters from Planck Collaboration et al. (2016b).

The re-simulation process initializes the parent dark matter particles into dark matter $m_{\text{DM}} = 1.27 \times 10^9 h^{-1} M_{\odot}$ and gas components $m_{\text{gas}} = 2.36 \times 10^8 h^{-1} M_{\odot}$, then conduct three different baryonic codes: GADGET-MUSIC (Sembolini et al. 2013), GADGET-X (Rasia et al. 2015), and GIZMO-SIMBA (Davé et al. 2019; Cui et al. 2022). Thanks to THE300's unique setups, for example, the large surrounding area of the central cluster, the filamentary structures connecting to the cluster are studied (Kuchner et al. 2020; Rost et al. 2021; Kuchner et al. 2021; Rost et al. 2024); the large sample of clusters permits statistical studies on cluster profiles (Mostoghiu et al. 2019; Li et al. 2020; Baxter et al. 2021), back-splash galaxies (Arthur et al. 2019; Hagggar et al. 2020; Knebe et al. 2020), cluster dynamical state (De Luca et al. 2021; Capalbo et al. 2021; Zhang et al. 2022; Li et al. 2022), lensing studies (Vega-Ferrero et al. 2021; Herbonnet et al. 2022; Euclid Collaboration et al. 2023) and cluster mass (Li et al. 2021; Gianfagna et al. 2023); it is further used for the machine learning studies (de Andres et al. 2022, 2023; Ferragamo et al. 2023).

In this paper, we only focus on the results from GADGET-X and GIZMO-SIMBA runs. We do not consider GADGET-MUSIC due to its lack of AGN feedback, which results in an overabundance of massive galaxies compared to actual observations (see Fig.7 in Cui et al. 2018). That is unrealistic and will significantly alter the MR relation with a higher galaxy stellar mass cut. For details of the two simulation models we study, we refer to Cui et al. (2018, 2022) for the general comparisons and the references therein for more information on the detailed implementation of the baryon models. Here, we briefly mention that the former is mostly calibrated based on gas properties, which present better agreement to the observation in gas properties, such as density/temperature profiles (Li et al. 2020, 2023). While the latter is calibrated based on the stellar properties as described in Cui et al. (2022). Nevertheless, the cluster's global properties are very similar.

2.2. the halo and galaxy catalogues

We utilize four snapshots, corresponding to redshifts $z = [0, 0.5, 1, 1.5]$, for all the halos within the 324 cluster regions.

Within each region, halos are first identified by AHF (Knollmann & Knebe 2009), a halo finder based on the spherical overdensity (SO) algorithm. We only consider halos with mass $M = M_{200c} > 1 \times 10^{13} h^{-1} M_{\odot}$, where M_{200c} is defined as the mass enclosed within a radius R_{200c} where the average density is 200 times the critical density at the redshift of the halo.

Galaxies within these halos are further identified by Caesar, based on a 6-dimensional friends-of-friends (6DFOF) algorithm. Considering the resolution, we only include galaxies with stellar mass $M_{\star} \geq 10^{9.5} h^{-1} M_{\odot}$, to ensure at least 10 stellar particles per galaxy. Additionally, we also exclude those host halos which are contaminated by low-resolution particles.

In Figure 1, we show the cumulative satellite stellar mass functions (CSSMF), which represent the total number of satellite galaxies with stellar masses greater than M_{\star} per cluster. The CSSMFs are derived from all the selected halos binned in different halo masses (different color lines). Different redshift results are shown in different columns. It is interesting to see that the CSSMFs scale almost perfectly with host halo mass as shown in the bottom row at all galaxy stellar masses, albeit only little variations at the massive galaxy stellar mass end. Though the lines are still parallel to the horizontal golden line, the exact constant values seem to vary (get closer to the golden line) slightly from low to high redshift, $z = 1.5$. The two simulations are also in very perfect agreement, except for the tiny change at

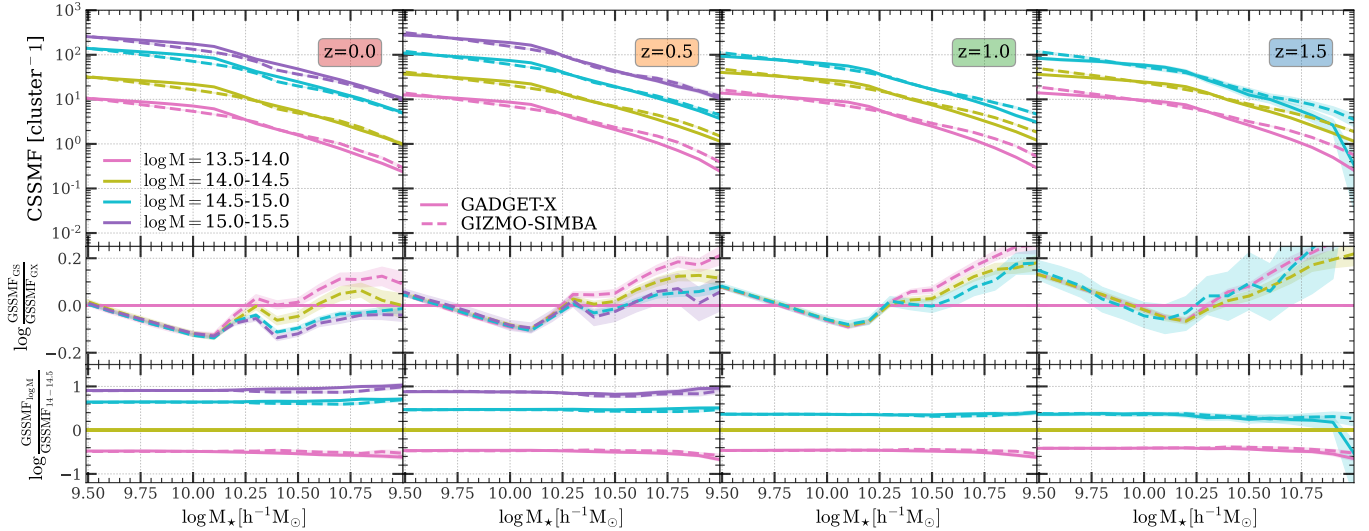


Figure 1. Cumulative satellite galaxy stellar mass function (CSSMF) per cluster, from the GADGET-X (solid lines) and the GIZMO-SIMBA (dashed lines) simulations at different redshifts and for different halo mass bins. The shaded regions show 68 percent confidence intervals from bootstrap resampling. From left to right, each column corresponds to redshift $z = [0, 0.5, 1.0, 1.5]$, respectively, and different colors represent different halo mass bins as indicated in the legend. The second row shows the difference in logarithmic CSSMF between the two simulations. The third row represents the difference in logarithmic CSSMF between a given halo mass bin and the one displayed as the yellow line.

$M_* \gtrsim 10^{10.25} h^{-1} M_\odot$. This suggests that the slope of the MR relation will be quite similar between the two simulations but decreases weakly with the redshift.

The absolute differences between GADGET-X and GIZMO-SIMBA are shown in the middle row, which clearly depend on the galaxy’s stellar mass. And this dependence is also tangled with the host halo masses at higher galaxy stellar mass, $M_* \gtrsim 10^{10} h^{-1} M_\odot$. This dependence further evolves with redshift as well: Although the first deep’s position – at $\sim 10^{10.1} h^{-1} M_\odot$ corresponding to the crossing point in Fig. 8 in Cui et al. (2022) – is more or less stable at different redshifts, the relative difference curves shift up as redshift increasing to $z = 1.5$; The middle peak at around $\sim 10^{10.3} h^{-1} M_\odot$ at $z = 0$ is getting weaker and almost disappeared at higher redshift. This mostly connects to the relative difference between GADGET-X and GIZMO-SIMBA on the normalization parameter of the MR relation, while this normalization parameter is determined by the values of the CSSMFs which are presented on the top row of Figure 1.

It is interesting to note that there is a small increase of CSSMF within the same halo mass bin tracking back to higher redshifts. This could be caused by several reasons, e.g. the pseudo halo evolution resulting from the fact that we are using R_{200c} ; the halo evolution which changes its density profile either because of accretion or merger. We made a simple comparison between the simulated and analytical $R_\zeta \equiv R_{200c}(z = 1)/R_{200c}(z = 0)$ with a concentration parameter from Duffy et al. (2008)

and found that the simulated R_ζ is larger than the analytical one, which suggests that the halo evolution plays a major role in this CSSMF in agreement with Ahad et al. (2021). This can be simply explained as the halos are still in the formation process through mergers at high redshift, which can also be viewed as the relaxation fraction of the cluster’s dynamical state drops along the redshift (see De Luca et al. 2021, for example).

Magnitudes of the galaxies are also provided by Caesar, using the flexible stellar population synthesis code FSPS (Conroy et al. 2009; Conroy & Gunn 2010). Dust obscuration is also taken into account in this study for GIZMO-SIMBA, because it has the dust model included (see Li et al. 2019). However, there is no dust attenuation for GADGET-X. We don’t include that for GADGET-X for two reasons: (1) there is very little dust in these cluster satellite galaxies, which has especially been verified in GIZMO-SIMBA; (2) simple dust attenuation laws, such as Charlot & Fall (2000), will only affect the magnitude systematically for all the galaxies at a particular band. So, it will have minimal effect on our results. For example, at $z = 0$, only 4.6% of galaxies exhibit a fractional difference greater than 0 between the CSST i band absolute magnitudes considering dust and without considering dust, while, only 2.06% of galaxies have a fractional difference greater than 0.01. More complex models require a lot of assumptions, which may not be worth it given that dust contributes little in the cluster environment suggested by GIZMO-SIMBA. Our analysis focuses mainly on the

ongoing and upcoming large optical surveys, namely the Chinese Space Station Telescope (CSST, Zhan 2011), and Euclid (Laureijs et al. 2011). Specifically, we consider the CSST i-band and z-band magnitudes, as well as the Euclid h-band magnitude in this study. We note here that the simulation used in this paper may not be able to reach the Euclid limits at low redshift (see Jiménez Muñoz et al. 2023). However, this is not a major concern for our MR relation study, because (1) we are studying different magnitude/stellar mass limits, above which all galaxies are included; (2) our results have a better convergence with low limits, such that it would be safe to extend our conclusions/fitting parameters to an even lower limit.

3. METHOD

3.1. model

In the absence of non-gravitational physical processes during cluster formation, cluster scaling relation will follow a self-similar model prediction (Kaiser 1986). The self-similar model predicts power-law scaling relations, which have been used in many simulations and observational studies.

$$\langle \ln \lambda | \ln M \rangle = A + B \ln \left(\frac{M}{M_{piv}} \right), \quad (1)$$

where λ is the optical richness defined in the last section, A is the normalization, B is the slope with respect to the halo mass M , and $M_{piv} = 3 \times 10^{14} h^{-1} M_{\odot}$ is a pivot mass scale.

We adopt forward modeling for the probability distribution function of optical richness for halos with a given mass $P(\lambda|M)$. The corresponding backwards $P(M|\lambda)$ has also been studied in many works (e.g. Simet et al. 2017). The former allows for a more direct comparison of the model prediction with the measurements, while the latter is more suitable for inferring halo mass from observables. These two can be converted into each other by using the halo mass function (Evrard et al. 2014). Note that, modeling the $P(M|\lambda)$ is different from modeling the $P(\lambda|M)$. This is because the M in observation is subject to many systematics. Directly transferring from $P(\lambda|M)$ to $P(M|\lambda)$ needs Bayes theorem:

$$P(M|\lambda) = \frac{P(\lambda|M)P(M)}{P(\lambda)},$$

where $P(M)$ is related to the halo mass function. Evrard et al. (2014) gave an approximate solution: if $P(\ln \lambda | \ln M)$ is Gaussian with a scatter $\sigma_{\ln \lambda}$, $P(\ln M | \ln \lambda)$ will be Gaussian with a scatter $\sigma_{\ln M} = \sigma_{\ln \lambda} / B$ in the first order assuming $P(M)$ is simple power law and $P(\lambda)$ is a constant.

Typically, $P(\lambda|M)$ is modeled as a log-normal distribution (Murata et al. 2018, 2019). However, this form exhibits a negative skewness (Anbajagane et al. 2020), which is also expected from the HOD model. In the HOD model, galaxies are categorized as central and satellite galaxies $\lambda = \lambda^{\text{cen}} + \lambda^{\text{sat}}$. The latter follows a sub-Poisson distribution at small occupation numbers and a super-Poisson distribution at large numbers (Jiang & van den Bosch 2017). In the mass range we selected later, there is always a central galaxy with $\lambda^{\text{cen}} = 1$, and the distribution for satellite galaxies is chosen to be super-Poisson because we are interested in galaxy clusters.

We model the deviation from Poisson as a Gaussian distribution with scatter σ_{I} (Costanzi et al. 2019), which represents halo-to-halo variations influenced by the large-scale environments (Mao et al. 2015). Specifically, the richness can be written as $\lambda = \lambda^{\text{cen}} + \lambda^{\text{sat}} = 1 + \Delta^{\text{Poisson}} + \Delta^{\text{Gauss}}$, where Δ^{Poisson} follows a Poisson distribution with a mean value of $\langle \lambda^{\text{sat}} \rangle$, and Δ^{Gauss} follows a Gaussian distribution with a mean of 0 and a scatter of σ_{I} .

To obtain the probability distribution $P(\lambda)$, we sample λ 10^6 times for each $\{\langle \lambda^{\text{sat}} \rangle, \sigma_{\text{I}}\}$. Then, we fit $P(\lambda)$ with a skewed Gaussian distribution by calibrating the parameters $\{\sigma, \alpha\}$:

$$P(\lambda | M) = \frac{1}{\sqrt{2\pi\sigma^2}} e^{-\frac{(\lambda - \langle \lambda^{\text{sat}} | M \rangle)^2}{2\sigma^2}} \text{erfc} \left[-\alpha \frac{\lambda - \langle \lambda^{\text{sat}} | M \rangle}{\sqrt{2\sigma^2}} \right], \quad (2)$$

where $\langle \lambda^{\text{sat}} \rangle = \exp(\ln \lambda) - 1$. For the subsequent calculations, we employ two-dimensional interpolation tables that relate $\{\langle \lambda^{\text{sat}} \rangle, \sigma_{\text{I}}\}$ to the corresponding values of $\{\sigma, \alpha\}$ as shown in Figure 2.

Figure 3 shows an example utilizing this skewed Gaussian function to fit the richness probability distribution from the GADGET-X data in two mass bins at $z = 0$, while also employing the commonly used log-normal function for comparison. The richness here is defined as the count of all member galaxies in the catalogue described in Section 2.2. The former demonstrates better incorporation of low richness values, while both exhibit greater consistency in the larger mass bin $\log M [h^{-1} M_{\odot}] = [14.8, 14.85]$. Additionally, regardless of the mass bin, the residual of the former is consistently lower than that of the latter: $2.48 < 3.64$ for $\log M [h^{-1} M_{\odot}] = [13.9, 13.95]$ and $15.53 < 15.96$ for $\log M [h^{-1} M_{\odot}] = [14.8, 14.85]$. More comparisons for different galaxy selections and for GIZMO-SIMBA are shown in the Appendix A.

However, these two panels are fitted separately, which means that the mass dependence of the scatter is not taken into account. For the scatter of the skewed Gaus-

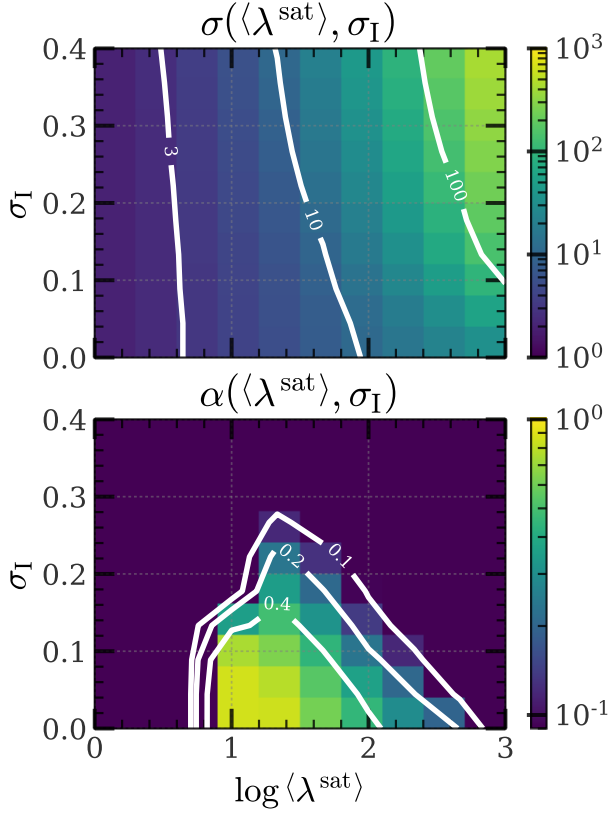


Figure 2. Two-dimensional interpolation tables for σ_I (upper panel) and α (lower panel) as a function of $\{\langle \lambda^{\text{sat}} \rangle, \sigma_I\}$.

sian distribution σ_I , we will subsequently demonstrate that it exhibits no mass dependence. While for the scatter of the log-normal distribution, there is a widely used form (Capasso et al. 2019; Bleem et al. 2020; Costanzi et al. 2021):

$$\sigma_{\ln \lambda}^2 = \sigma_{\text{IG}}^2 + \left(e^{\langle \ln \lambda \rangle} - 1 \right) / e^{2\langle \ln \lambda \rangle}, \quad (3)$$

i.e., the sum of a constant intrinsic scatter with a Poisson-like term. This form incorporates the mass dependence through the Poisson term, which is also motivated by the super-Poisson distribution in the HOD model. However, compared to our approach, it simplifies this assumption, resulting in an extra mass dependence. We will demonstrate this from two perspectives.

On the one hand, starting from sampling, we select a set of $\{\langle \lambda^{\text{sat}} \rangle, \sigma_I\}$, sample a population of λ , calculate the mean $\langle \ln \lambda \rangle$ and variance $\sigma_{\ln \lambda}^2$ of $\ln \lambda$, and then subtract the scatter contributed by the Poisson distribution to obtain $\sigma_{\text{IG}}^2 = \sigma_{\ln \lambda}^2 - (e^{\langle \ln \lambda \rangle} - 1) / e^{2\langle \ln \lambda \rangle}$. Figure 4 presents the derived values of σ_{IG} . Overall, σ_{IG} is larger than σ_I and exhibits a clear mass dependence. Even when considering only clusters with $\lambda > 20$, as done in Capasso et al. (2019) Bleem et al. (2020) and Costanzi

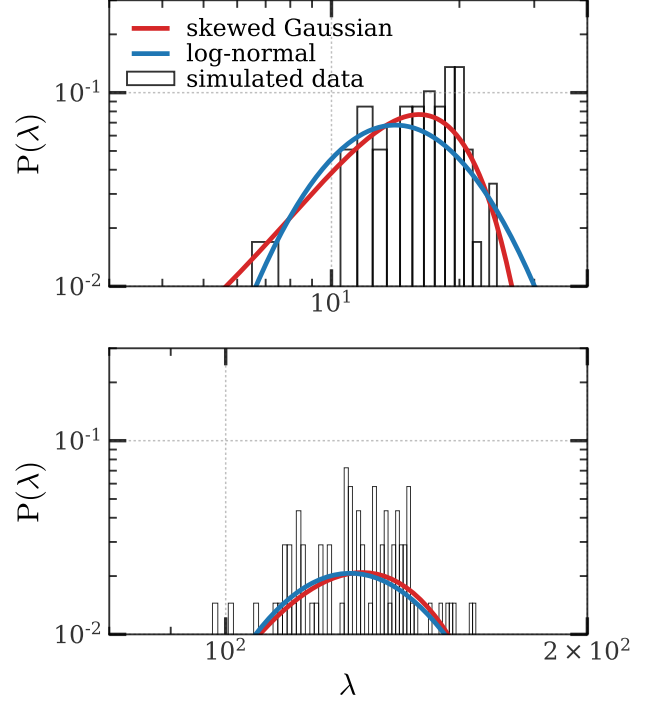


Figure 3. Richness distribution (black) for GADGET-X at $z = 0$, as well as two fitting probability functions: skewed Gaussian (red) and log-normal (blue) function. The upper and lower panels correspond to mass bin $\log M[h^{-1}M_{\odot}] = [13.9, 13.95]$ and $\log M[h^{-1}M_{\odot}] = [14.8, 14.85]$, respectively.

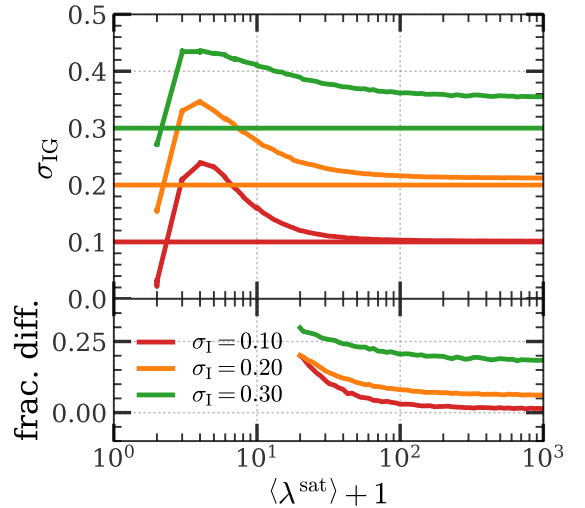


Figure 4. Richness (mass) dependence of σ_{IG} derived from sampling. Each color represents a different value of σ_I as indicated in the legend. The second row illustrates the fractional difference between σ_{IG} and σ_I .

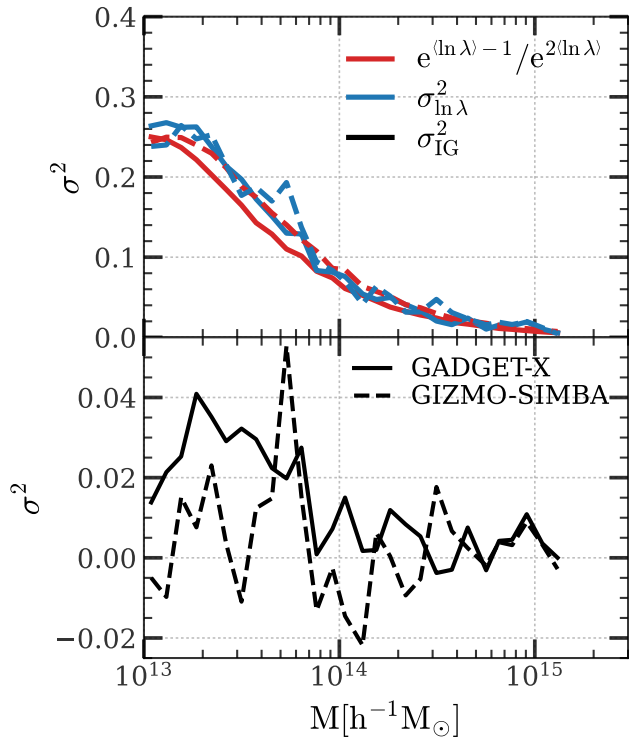


Figure 5. Richness (mass) dependence of σ_{IG} derived from simulation data at $z = 0$. The upper panel shows the Poisson term (red) and the variance (blue). The lower panel presents the derived intrinsic scatter (black) in the log-normal distribution. Solid lines correspond to the GADGET-X simulation, while dashed lines correspond to the GIZMO-SIMBA simulation.

et al. (2021), a weak mass dependence still remains. Neglecting this dependence would lead to an overestimation of σ_{IG} . In the subsequent section, for the purpose of comparison with the existing literature, we choose to ignore the mass dependence of σ_{IG} .

On the other hand, starting from the simulation data we divide clusters into several mass bins, calculate $\langle \ln \lambda \rangle$ and $\sigma_{\ln \lambda}$ in each bin, and then estimate the Poisson term and σ_{IG} as shown in Figure 5. Figure 5 indicates a significant mass dependence of σ_{IG} for GADGET-X, which is similar to Figure 4. While σ_{IG}^2 for GIZMO-SIMBA fluctuates around 0, implying that the richness in GIZMO-SIMBA closely follows a Poisson distribution.

In summary, the skewed Gaussian distribution outperforms the log-normal distribution even without accounting for mass dependence. Additionally, the scatter of the log-normal distribution σ_{IG} exhibits a nonlinear mass dependence, and neglecting this dependence would lead to an overestimation of the scatter. Therefore, we opt to model using the skewed Gaussian function with a scatter σ_{I} . At last, the same distribution function is

applied to both M_* and Magnitude limits. As shown in Appendix A, this skewed Gaussian function also provides a good fit to the data with magnitude limit in Figure 14.

3.2. fitting procedure

We define the richness λ as the count of member galaxies satisfying specific selection thresholds within a halo of radius R_{200c} . We consider two kinds of thresholds for member selection: (1) galaxy stellar mass M_* , and (2) galaxy absolute magnitude in the CSST i-band \mathcal{M}_i .

For each redshift and galaxy selection, we set distinct halo mass limits M_{limit} that ensure the fraction of halos with a richness less than 10 $f_{\lambda < 10}$ remains below 0.1 within each halo mass bin. We adopt this criteria for two primary reasons: (1) The corresponding M_{limit} value is approximately $5 \times 10^{13} - 6 \times 10^{14} h^{-1} M_{\odot}$, which aligns with the typical mass of a cluster $\sim 10^{14} h^{-1} M_{\odot}$, and (2) a richness below 10 leads to deviations from a power-law form of scaling relation.

To estimate parameters $\{A, B, \sigma_{\text{I}}\}$, we fit to the data simultaneously using the Python package *emcee*, a Markov Chain Monte Carlo (MCMC) ensemble sampler developed by Foreman-Mackey et al. (2013). In Figure 6, we show an example of the MR relation for GADGET-X with $M_* \geq 10^{9.5} h^{-1} M_{\odot}$ at $z = 0$. The data points are coming from the simulation and the red line and shaded region are the fitting results.

Note that for larger M_* , not all redshifts have fitting results. This is due to the requirement on $d \log M$, the logarithmic halo mass difference between the largest halo mass and the halo mass limit M_{limit} , which has to be greater than 0.5. Below this value, there will not be sufficient data to constrain the slope parameter B . This plot confirms our fitting is working as expected, especially for the error estimation.

We have considered the mass dependence of σ_{I} and found it to be consistent with 0. Specifically, we model σ_{I} as $\sigma_{\text{I}} = \sigma_{\text{I0}} + q \times \ln(M/M_{\text{piv}})$, then fitted these four parameters $\{A, B, \sigma_{\text{I0}}, q\}$ and finally found $q \simeq 0$. So for brevity, we only consider three parameters $\{A, B, \sigma_{\text{I}}\}$ hereafter. Furthermore, we do not parameterize the redshift evolution of these parameters directly. Instead, we infer it from different redshifts $z = [0, 0.5, 1, 1.5]$ and then examine their evolution by determining the most suitable value of a posterior, which will be detailed later.

4. RESULTS

In this section, we present our main results on the MR relation based on the THE THREE HUNDRED cluster simulations. The richness can be measured with both stellar mass and magnitude limits on member galaxies.

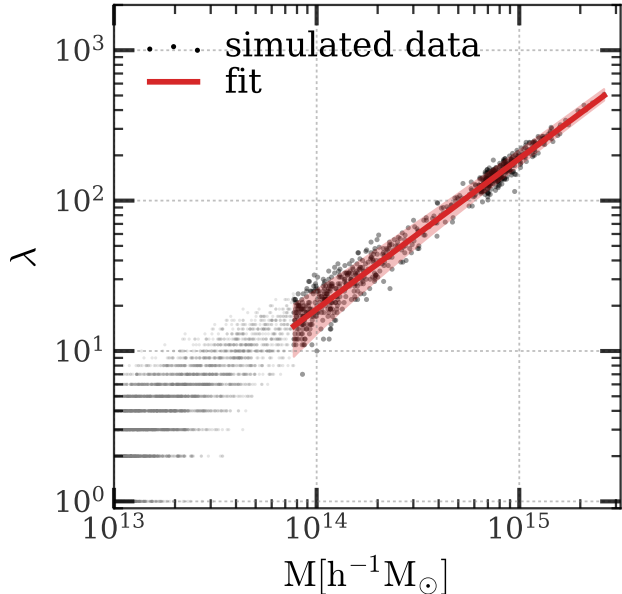


Figure 6. Mass-richness relation for GADGET-X at $M_* = 10^{9.5} h^{-1} M_\odot$ and $z = 0$. Each dot represents an individual halo. Smaller gray dots that do not satisfy $f_{\lambda < 10} < 0.1$ have been discarded. The red line represents the mean relation through the fitting of Equation 1, and the shaded area shows the 68% confidence region of the skewed Gaussian distribution of Equation 2.

We present the two cases separately in the following two subsections. With our fitting method described in the previous section, we only show the results of fitting parameters in this section.

4.1. MR relation with galaxy selection by stellar mass

For the richness based on galaxy selection by stellar mass, we adopt the galaxy stellar mass threshold M_* ranging from $10^{9.5} h^{-1} M_\odot$ to $10^{10.5} h^{-1} M_\odot$. The lower limit, $10^{9.5} h^{-1} M_\odot$, is determined by the simulation resolution (see Jiménez Muñoz et al. 2023). Considering that current survey can already observe galaxies with a stellar mass of $10^{10} h^{-1} M_\odot$ (Murata et al. 2019), our results with M_* in the range of $10^{9.5} - 10^{10} h^{-1} M_\odot$ will be informative for future surveys. For the upper limit, $10^{10.5} h^{-1} M_\odot$, we take a look at the satellite galaxy stellar mass function (SSMF). Figure 8 in Cui et al. (2022) illustrates an unrealistic peak at $10^{10.3} h^{-1} M_\odot$ in the SSMF for GADGET-X compared to the SDSS result (Yang et al. 2018), and a sharp decline around $10^{10.4} h^{-1} M_\odot$ for GIZMO-SIMBA, which is attributed to the AGN feedback treatment. Therefore, our results with M_* in the range of $10^{10} - 10^{10.5} h^{-1} M_\odot$ allow for a comparison of effects within this interval, which can further identify their influences on the MR relation. Above the stellar mass upper limit, we will have only a lim-

ited number of galaxies even in clusters, which will the fitting as described in the previous section.

In Figure 7, we present our main results on the fitting parameters $\{A, B, \sigma_1\}$ as a function of the stellar mass threshold at different redshifts depicted in different colors. Results from GADGET-X are presented with solid lines, while GIZMO-SIMBA with dashed lines. Shaded regions are the 68% confidence intervals. The relative differences between the two simulations and different redshifts are highlighted in the middle and bottom rows, respectively.

The amplitude A decreases with the stellar mass threshold for both simulations, which is expected. This is simply because the richness decreases as a higher stellar mass cut is applied. When $M_* \lesssim 10^{10} h^{-1} M_\odot$, we demonstrate that A is linearly correlated with $\log M_*$. While its redshift evolution can be modeled by constant values albeit the two different simulations exhibit different evolution trends and strengths, as illustrated in the middle- and lower-left panels of Figure 7. The constant shift indicates that there is almost no redshift evolution in the shape of the SSMF (Xu et al. 2022) below $M_* \lesssim 10^{10} h^{-1} M_\odot$. The amplitude A increases with redshift, which is in line with HOD results, and is mainly due to the process of hierarchical accretion (Kravtsov et al. 2004; Zheng et al. 2005; Contreras et al. 2017; Contreras & Zehavi 2023), see also Section 2 for more discussions on why A increases with redshift. We only note here that GIZMO-SIMBA exhibits a larger value of A at high redshifts and a smaller value at low redshifts, which can be attributed to early star formation and strong AGN feedback (Cui et al. 2022); While for GADGET-X, A remains relatively constant at high redshifts.

However, when $M_* \gtrsim 10^{10.25} h^{-1} M_\odot$, this behavior starts to be altered – the agreement between the two simulations is much better at all redshifts; while the redshift evolution depends on the galaxy stellar mass threshold with a tilt-up. This implies a redshift evolution in the shape of SSMF in this stellar mass range. This is in agreement with the CSSMF shown in Figure 1: for GADGET-X, the knee point changes from 10.1 to 10.2 when the redshift changes from 0 to 1.5. A similar behavior exists in GIZMO-SIMBA.

By looking at the top-central panel, the slope B remains almost constant for both simulations when $M_* \lesssim 10^{10} h^{-1} M_\odot$. Except for $z = 1.5$, the agreements between the two simulations are also very good. This can also be attributed to the curve of the CSSMF which only scales with the halo mass and shows weak dependence on redshift (Ahad et al. 2021). The slight discrepancy

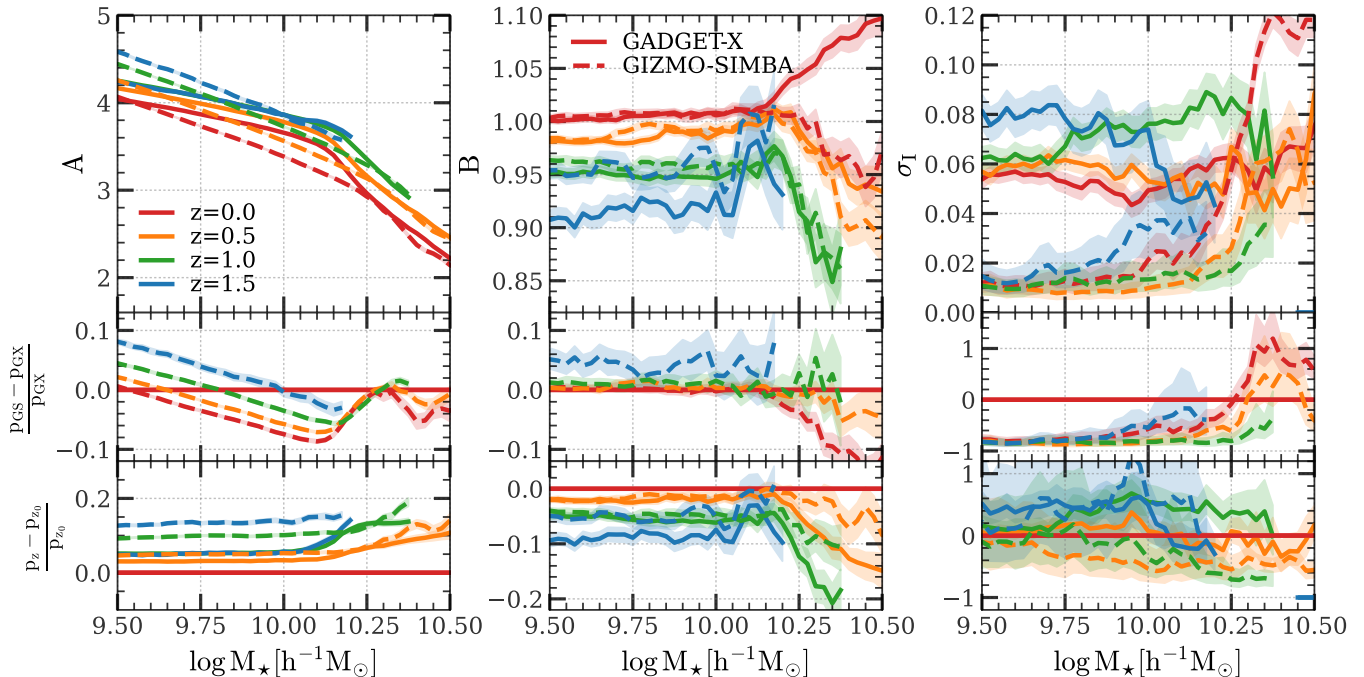


Figure 7. Fitting parameters $\{A, B, \sigma_I\}$ for the richness-mass distribution as functions of the galaxy stellar mass threshold M_* , derived from the GADGET-X (solid lines) and the GIZMO-SIMBA simulations (dashed lines). From left to right, the columns show A , B , and σ_I , respectively, and different colors represent different redshifts as indicated in the legend. Error bands represent the 68% confidence regions for the fitted parameters. The second row shows the fractional difference between the two simulations. The third row illustrates the fractional difference between different redshifts for each simulation.

between the two simulations at $z = 1.5$ can be attributed to the influence of M_{limit} . Since there are fewer large halos at high redshift, the slope B is more susceptible to M_{limit} . We have checked that increasing M_{limit} yielded greater consistency in the values of B between the two simulations at $z = 1.5$. As illustrated in the third row of Figure 1, before reaching $10^{10} h^{-1} M_\odot$, the difference between different halo mass bins remains constant with respect to M_* , and this consistency is observed in both GADGET-X and GIZMO-SIMBA simulations, which explains the agreement of B . However, after surpassing $10^{10} h^{-1} M_\odot$, the B values increase for GADGET-X at $z = 0$ and both simulations at $z = 1.5$, while its values decrease for the others. Therefore, the good agreement between the two simulations still exists except for $z = 0$. The reason can be explained as there are more galaxies in GIZMO-SIMBA than GADGET-X for lower halo mass, but less for higher halo mass at $z = 0$ as illustrated in Figure 1. While the difference between the two simulations is more or less consistent at other redshifts, i.e. GIZMO-SIMBA tends to have more galaxies in halos than GADGET-X with different masses. At last, the redshift evolution of B is also constant with $M_* \lesssim 10^{10} h^{-1} M_\odot$ and these constant values are also similar between the two simulations except for the highest redshift.

For GADGET-X over the entire range of M_* range, and for GIZMO-SIMBA at $M_* \gtrsim 10^{10.3} h^{-1} M_\odot$, the scatter σ_I remains relatively constant with M_* and similar between the two simulations. However, at $M_* \lesssim 10^{10} h^{-1} M_\odot$, GIZMO-SIMBA has a much lower σ_I compared to GADGET-X. Because this intrinsic scatter is dominated by the low-mass halos (see Figure 6), we think the richness in GIZMO-SIMBA tends to have a smaller scatter at low mass halos than GADGET-X. Though the intrinsic scatter in GIZMO-SIMBA shows weak dependence on stellar mass, the one in GADGET-X tends to present a weak increase with redshift rather than dependence on stellar mass. Taken together, these three dependencies collectively suggest that the intrinsic scatter is likely attributed to environmental factors (Mao et al. 2015).

For GADGET-X, σ_I demonstrates an increasing trend with redshift. For GIZMO-SIMBA, when $M_* \lesssim 10^{10} h^{-1} M_\odot$, σ_I remains below 0.02 at the 68% confidence level for all the redshifts, consistent with Figure 5. This suggests that the richness in GIZMO-SIMBA follows a nearly Poisson distribution, even at large occupation numbers. This behavior can be attributed to the intense baryonic processes in GIZMO-SIMBA, resulting in a negligible environmental impact relative to the strength of the baryonic processes. However, when

$M_\star \gtrsim 10^{10} h^{-1} M_\odot$, σ_I increases rapidly and shows a decreasing trend with redshift up to $z = 1$, which is opposite to the GADGET-X run.

In summary, when $M_\star \gtrsim 10^{10} h^{-1} M_\odot$, the behavior of parameters displays stronger influence by the baryon models. When $M_\star \lesssim 10^{10} h^{-1} M_\odot$, the dependence of our parameters, A and B , on redshift and stellar mass, is consistent with certain findings of the HOD studies at large (Kravtsov et al. 2004; Zheng et al. 2005; Contreras et al. 2017; Contreras & Zehavi 2023). However, comparing our results to Contreras et al. (2017) and Contreras & Zehavi (2023), there exist subtle differences in the redshift dependence. Specifically, our parameter A for GADGET-X remains roughly to be a constant at higher redshift, whereas their A demonstrates an increase with z which agrees better with GIZMO-SIMBA. Moreover, the slope B from observations remains a constant for redshifts greater than approximately 0.7, while our B shows a decreasing trend for both simulations. These distinctions could be attributed to different galaxy selections. In contrast to their approach of fixing the galaxy number density n for different redshifts, we maintain a fixed galaxy stellar mass threshold M_\star . We have checked that if we fix n , A exhibits an increasing trend with redshift. However, B , at least until $z = 1.5$, continues to show a downward trend which indicates the richnesses for different halo masses have fewer variations.

4.2. MR relation with galaxy selection by magnitude

Galaxy stellar mass is not a quantity that can be directly measured from observation. However, it is closely related to the galaxy’s luminosity or magnitude. As such, the richness can be also derived with selection of galaxies based on their magnitudes. In this subsection, we investigate the MR relation when the galaxy magnitude limit, instead of galaxy stellar mass limit, is used for controlling the richness.

We utilize limit on the absolute magnitude as the galaxy selection criteria, employing the CSST i-band \mathcal{M}_i with \mathcal{M}_i ranging from -18 to -23 . The fitting results of parameters $\{A, B, \sigma_I\}$ as functions of \mathcal{M}_i are depicted in Figure 8, which is similar to Figure 7. We just show the results of \mathcal{M}_i corresponding to the range of $M_\star = [10^{9.5}, 10^{10.5}] h^{-1} M_\odot$, and mark the point corresponding to $M_\star = 10^{10} h^{-1} M_\odot$ through the $M_\star - \mathcal{M}_i$ relation as shown in Section 5.1.

In general, if $\log M_\star$ is correlated with the magnitude without scatter, we would expect that the fitting parameters of the MR relation will be a simple shift from those with cuts on M_\star . By comparing Figure 8 and Figure 7, we find the conclusions in the previous sub-

section are qualitatively unchanged. More discussions on the $\log M_\star$ and magnitude relation can be found in Section 5.1. Here we focus on the subtle changes in the fitting parameters.

The dependence of A and B on redshift and galaxy threshold remains consistent with Section 4.1, with $M_\star \approx 10^{10} h^{-1} M_\odot$ serving as the dividing point. However, the redshift evolution around $M_\star \approx 10^{10} h^{-1} M_\odot$ seems to be not consistent with the fainter galaxy end, unlike what has been shown in Figure 7. $M_\star \approx 10^{10} h^{-1} M_\odot$ is more-or-less the separation part in the galaxy color bimodality plot, which contains both blue, star-forming and red, quenched galaxies. When $M_\star \geq 10^{10} M_\odot$, Fig.9 in Cui et al. (2022) exhibits a clear separation in the satellite galaxy color-magnitude diagram between GADGET-X and GIZMO-SIMBA with galaxies in GIZMO-SIMBA appearing blue. We know that a galaxy’s luminosity is strongly dependent on its color, as such, it is not surprising to see an increased scatter around that stellar mass, which results in an increase of σ_I for both GADGET-X and GIZMO-SIMBA as is shown in the third column. In addition, this separation varies with redshift because of more star-forming galaxies at higher redshift. With this additional dependence, i.e. more brighter galaxies at higher redshift, the redshift evolution behaves differently from the case with M_\star limits for all the three parameters.

5. DISCUSSIONS

5.1. conversion between M_\star and \mathcal{M}_i

Practical sky surveys employ the magnitude to select galaxies, rather than the stellar mass. However, it is not realistic to provide fitting results of $\{A, B, \sigma_I\}$ for all bands in all surveys. Consequently, we aim to investigate whether it is possible to derive MR relations based on different galaxy magnitudes from a single MR relation using the M_\star threshold in Section 4.1. To accomplish this, we naturally turn to the galaxy stellar mass-absolute magnitude relation $M_\star - \mathcal{M}$ and specifically focus on the CSST i-band \mathcal{M}_i as an illustrative example.

We use a simple linear relation $\ln M_\star = A_i + B_i \mathcal{M}_i + C_i \ln(1+z)$, along with a Gaussian probability function $P(\ln M_\star | \mathcal{M}_i)$ incorporating a magnitude-redshift-independent scatter σ_i , to model the $M_\star - \mathcal{M}_i$ relation. The four parameters $\{A_i, B_i, C_i, \sigma_i\}$ are simultaneously fitted using the same procedure described in Section 3.2, but with galaxies as the input data. The resulting $M_\star - \mathcal{M}_i$ relations, without showing σ_i , for GADGET-X and GIZMO-SIMBA are as follows, re-

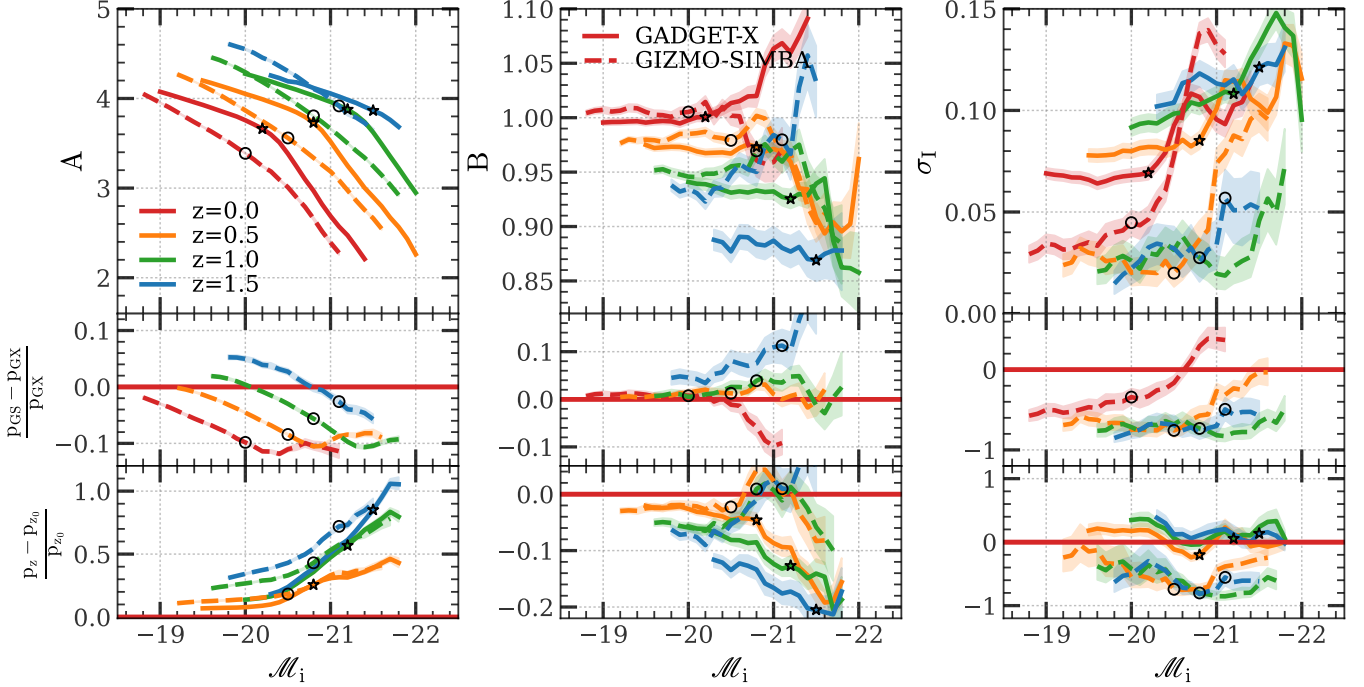


Figure 8. Fitting parameters $\{A, B, \sigma_1\}$ for the richness-mass distribution as functions of the threshold on galaxy’s absolute magnitude in the CSST i-band \mathcal{M}_i . Labels and legends are the same as Figure 7. Star markers (circle markers) correspond to $M_\star = 10^{10} h^{-1} M_\odot$ according to the $M_\star - \mathcal{M}_i$ relation (Equation 4) for GADGET-X(GIZMO-SIMBA).

spectively:

$$\begin{aligned} \ln M_\star &= 4.63 - 0.91 \mathcal{M}_i - 1.30 \times \ln(1+z), \\ \ln M_\star &= 4.49 - 0.93 \mathcal{M}_i - 1.10 \times \ln(1+z). \end{aligned} \quad (4)$$

An example has been shown in Figure 9 at $z = 0$. By employing this relation, we convert \mathcal{M}_i into M_\star as the selection criteria. The corresponding results are depicted by the dotted lines in Figure 10. The solid lines, on the other hand, represent the outcomes obtained directly using \mathcal{M}_i .

Parameters $\{A, B\}$ obtained from these two selections exhibit consistency within a fractional difference of 5% across the entire range, especially small with $M_\star \lesssim 10^{10} h^{-1} M_\odot$. It is worth noting that B with magnitude limit has a consistently lower value compared to the one with M_\star limit, the difference increases with redshift. In addition, the scatter σ_1 obtained using \mathcal{M}_i is significantly larger than the scatter σ_1 obtained using M_\star . This difference arises due to the presence of scatter in the $M_\star - \mathcal{M}_i$ relation, which increases σ_1 by approximately 50%. As indicated in the previous section, the large scatter as well as the redshift dependence of the parameters closely connect with the galaxy formation, especially the galaxy quenching event. As such, directly using the MR fitting result with magnitude cuts to estimate halo masses should be careful, an improper simulation, especially one that can not provide a faithful

galaxy color-magnitude diagram at multiple redshifts, may lead to biased results.

Nevertheless, these findings based on our simulations indicate that it is feasible to derive magnitude threshold results from stellar mass threshold results by utilizing the stellar mass-magnitude $M_\star - \mathcal{M}_i$ relation. Importantly, these conclusions are applicable not only for GADGET-X in CSST-i band, but also in other bands, as well as for GIZMO-SIMBA. A comprehensive presentation of these results is provided in the appendix.

It is noteworthy that the $M_\star - \mathcal{M}_i$ relation fitted from the simulation is based on the FSPS code, in which we select the initial mass function (IMF) of Chabrier (2003), consistent with both simulations’ setups. Adopting different IMFs will change the galaxy’s magnitude (e.g. Cappellari et al. 2012; Narayanan & Davé 2012; Bernardi et al. 2018). Generally speaking, the top-heavy IMF is found in regions of elevated star formation rate (e.g. Gunawardhana et al. 2011), which will yield more light in high energy bands.

5.2. 7-parameters relation

From this section, we focus only on the range of $M_\star = 10^{9.5} - 10^{10} h^{-1} M_\odot$, considering the current and future survey limits and the clearer stellar mass trends before $10^{9.5} h^{-1} M_\odot$ in the Figure 7.

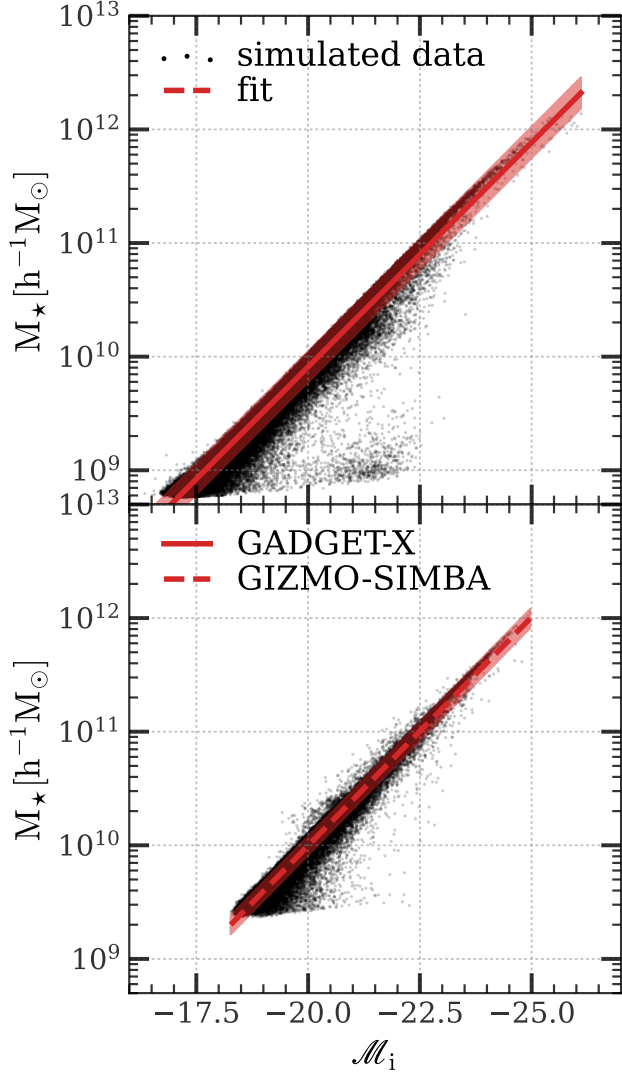


Figure 9. Galaxy stellar mass-absolute magnitude M_* – \mathcal{M}_i relation for GADGET-X (the upper panel) and GIZMO-SIMBA (the lower panel) in CSST i-band at $z = 0$. Each dot represents an individual galaxy. The red line represents the mean relation Equation (4), and the contour indicates the 68% confidence region of the Gaussian error.

We consider two distributions as mentioned previously, a skewed Gaussian distribution $P(\lambda)$ (Equation (2)) with the scatter σ_I , and a log-normal distribution $P(\ln \lambda)$ with the scatter σ_{IG} . We refer interesting readers to Appendix B for detailed comparisons. Despite the small scatter for GIZMO-SIMBA, we still utilize both distributions because different distributions have an impact on the fitting of parameters A and B .

In Section 4.1, we have presented the redshift and stellar mass dependencies. Now, we incorporate both

dependencies into the calculation:

$$\begin{aligned} A &\rightarrow A_0 + A_z \times \ln \frac{1+z}{1+z_p} + A_* \times \ln \frac{M_*}{M_{*p}}, \\ B &\rightarrow B_0 + B_z \times \ln \frac{1+z}{1+z_p}, \\ \sigma_I &\rightarrow \sigma_{I0} + \sigma_z \times \ln \frac{1+z}{1+z_p}, \end{aligned} \quad (5)$$

for the skewed Gaussian distribution, and:

$$\begin{aligned} A &\rightarrow A_0 + A_z \times \ln \frac{1+z}{1+z_p} + A_* \times \ln \frac{M_*}{M_{*p}}, \\ B &\rightarrow B_0 + B_z \times \ln \frac{1+z}{1+z_p}, \\ \sigma_{IG} &\rightarrow \sigma_{IG0} + \sigma_z \times \ln \frac{1+z}{1+z_p}, \end{aligned} \quad (6)$$

for the log-normal distribution, where $z_p = 0.5$, $M_{*p} = 1 \times 10^{10} h^{-1} M_\odot$.

Now there are a total of 7 parameters, namely $\{A_0, A_z, A_*, B_0, B_z, \sigma_{I0}, \sigma_z\}$ or $\{A_0, A_z, A_*, B_0, B_z, \sigma_{IG0}, \sigma_z\}$. These 7 parameters replace the 3 parameters used previously, and we repeat the fitting procedure for all clusters at redshifts $z = [0, 1.5]$ with a redshift interval of $dz = 0.5$. We set galaxy stellar mass thresholds of $M_* = [10^{9.5}, 10^{10}] h^{-1} M_\odot$ with a mass interval of $d \log M_* = 0.025$. To better capture the redshift evolution, we perform piecewise fitting for different redshift intervals. The results of these fits are presented in Table 1 and Figure 11 for GADGET-X, and Table 2 and Figure 12 for GIZMO-SIMBA.

In general, there are almost neglectable differences for both A and B fitting parameters between 3- and 7-parameter fitting. σ_I shows a slightly larger between the two fittings. Nevertheless, the largest increase from $\log M_* = 10 h^{-1} M_\odot$ is still within 0.02, which could be caused by the sample difference.

Compared to the scatter σ_I fitted by the skewed Gaussian distribution, the scatter σ_{IG} fitted by the log-normal distribution is larger as we expect. Additionally, the log-normal distribution tends to produce larger values for the amplitude A and smaller values for the slope B .

A_* remains constant across all redshift ranges. This indicates that there is no dependence between redshift and the stellar mass dependence of A , as we illustrated before. On the other hand, A_z and B_z exhibit slight variations among different redshift ranges, particularly for GADGET-X at $z = [1, 1.5]$. This suggests that a linear fit of the redshift may not be the optimal choice, but for the subsequent comparison, a linear fit of $z = [0, 1]$ is still employed.

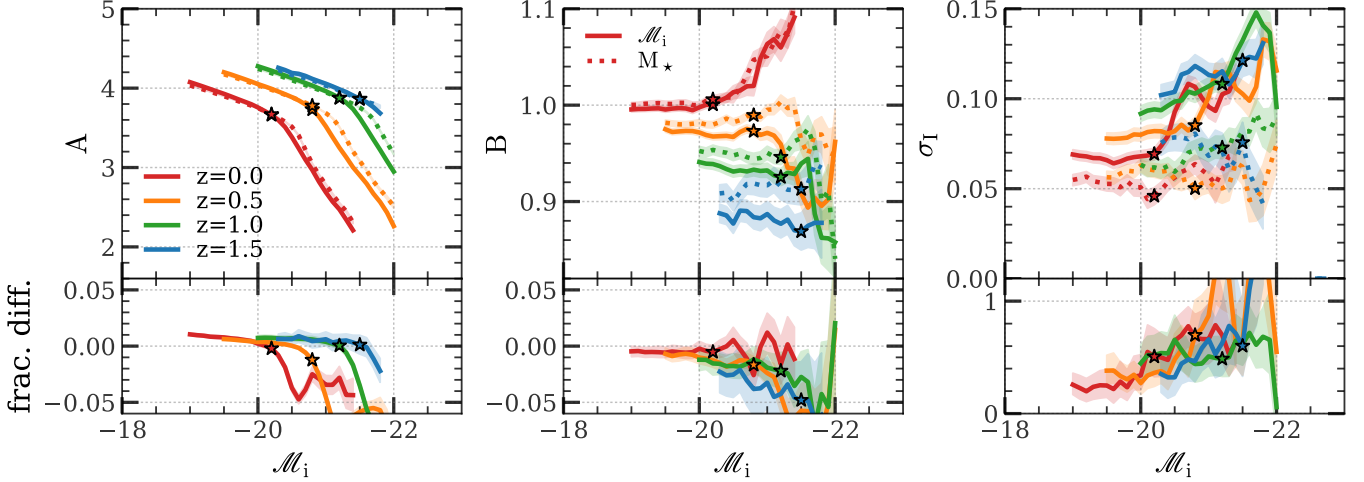


Figure 10. Fitting parameters $\{A, B, \sigma_I\}$ varying with the absolute magnitude \mathcal{M}_i , just for GADGET-X. Solid lines correspond to galaxies directly selected using \mathcal{M}_i , while dotted lines represent galaxies selected based on M_* converted from \mathcal{M}_i using Equation (4). From left to right, each column corresponds to the properties A , B , and σ_I , respectively, and different colors indicate different redshifts as indicated in the legend. Error bars represent the standard deviation from the fitted parameter value. The second row illustrates the fractional difference between these two selection methods. The black star points denote $M_* = 10^{10} h^{-1} M_\odot$.

Table 1. The 7 fitting parameters for GADGET-X. The upper panel displays the results obtained using the skewed Gaussian distribution, while the lower panel shows the results obtained using the log-normal distribution. Each column corresponds to a different redshift range. Fitting errors smaller than 10% have been omitted for a cleaner presentation.

z	[0,1]	[0,0.5]	[0.5,1]	[1,1.5]
A_0	3.792	3.803	3.800	3.887
A_z	0.205	0.245	0.150	$-0.017^{+0.006}_{-0.006}$
A_*	-0.320	-0.319	-0.323	-0.325
B_0	0.980	0.981	0.980	0.993
B_z	-0.031	-0.042	-0.060	-0.083
σ_{I0}	0.060	0.059	0.059	0.048
σ_z	$0.008^{+0.001}_{-0.001}$	$0.008^{+0.002}_{-0.002}$	$0.009^{+0.002}_{-0.002}$	$0.029^{+0.004}_{-0.004}$
A_0	3.819	3.833	3.829	3.911
A_z	0.196	0.244	0.128	$-0.028^{+0.006}_{-0.007}$
A_*	-0.314	-0.313	-0.316	-0.318
B_0	0.957	0.959	0.958	0.952
B_z	-0.044	-0.056	-0.084	-0.072
σ_{IG0}	0.067	0.063	0.063	0.066
σ_z	0.019	$0.011^{+0.002}_{-0.002}$	0.026	$0.021^{+0.005}_{-0.004}$

5.3. comparison with previous work

In this section, we present a comparative analysis of our results with various forward-modeling studies conducted by different surveys.

Capasso et al. (2019) and Chiu et al. (2023) utilize a cluster sample selected by X-ray and confirmed by opti-

Table 2. Similar to Table 1, but for GIZMO-SIMBA. Scatter parameters have been omitted because of the incomplete posterior distribution.

z	[0,1]	[0,0.5]	[0.5,1]	[1,1.5]
A_0	3.575	3.584	3.575	3.596
A_z	0.360	0.383	0.330	0.271
A_*	-0.594	-0.589	-0.602	-0.616
B_0	0.984	0.985	0.985	0.978
B_z	-0.037	-0.041	-0.057	$-0.040^{+0.004}_{-0.004}$
A_0	3.617	3.627	3.621	3.638
A_z	0.353	0.382	0.316	0.268
A_*	-0.581	-0.578	-0.585	-0.599
B_0	0.960	0.962	0.962	0.943
B_z	-0.043	-0.048	-0.069	$-0.030^{+0.005}_{-0.004}$

cal data. The former study uses galaxy dynamical information while the latter uses cluster abundance (referred to as number counts, NC) to calibrate the MR relation. Bleem et al. (2020) has a similar approach to Chiu et al. (2023), but instead of X-ray, they utilize the SZ effect. Additionally, Costanzi et al. (2021) incorporates other observable-mass relations (OMR) to supplement the information.

These studies adopt different mass definitions and relation forms. To facilitate comparison, we convert their respective cluster mass definitions to $M = M_{200c}$ by assuming a Navarro, Frenk, and White (NFW) profile (Navarro et al. 1997) and employing the concentration-mass relation from Duffy et al. (2008). We then cal-

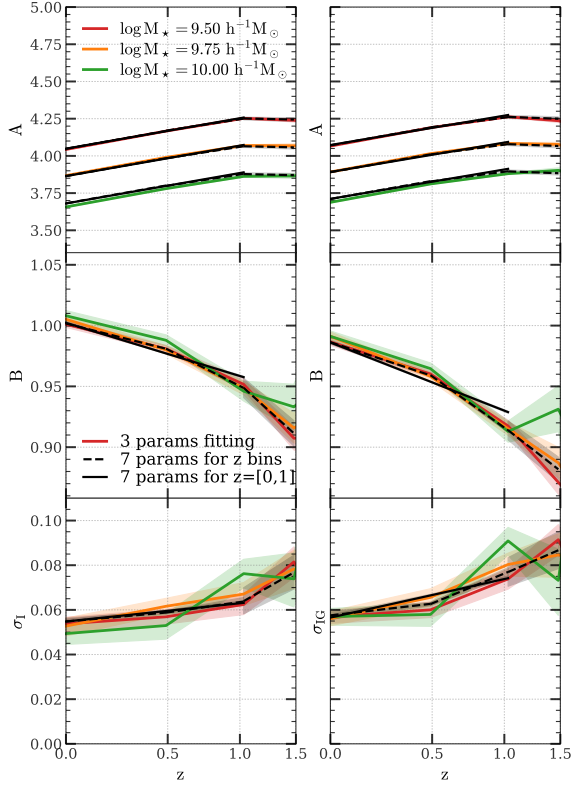


Figure 11. Fitting results for GADGET-X. The left panel displays the results obtained using the skewed Gaussian distribution, while the right panel shows the results obtained using the log-normal distribution. Colored lines represent the 3-parameters fitting performed at specific redshifts and stellar mass thresholds, as done in Section 4. Black lines represent the 7-parameters fitting conducted over a range of redshifts (dashed lines for $z = [0, 0.5]$, $[0.5, 1]$ and $[1, 1.5]$) and stellar mass thresholds, as described in this section.

culate the richness, as well as the dependence of richness on mass and redshift around the pivot point $M_p = 3 \times 10^{14} h^{-1} M_\odot$, $z_p = 0.5$, based on the different redshift and richness ranges reported in the literature. More specifically, we define:

$$\begin{aligned} \lambda_p &\equiv \lambda(M_p, z_p), \\ B_p &\equiv \frac{\ln \lambda(M_2, z_p) - \ln \lambda(M_1, z_p)}{2\Delta_{\ln M}}, \\ C_p &\equiv \frac{\ln \lambda(M_p, z_2) - \ln \lambda(M_p, z_1)}{2\Delta_{\ln(1+z)}}, \end{aligned} \quad (7)$$

with small enough steps $\Delta_{\ln M} = \ln \frac{M_2}{M_p} = \ln \frac{M_p}{M_1} = 0.001$ and $\Delta_{\ln(1+z)} = \ln \frac{(1+z_2)}{(1+z_p)} = \ln \frac{(1+z_p)}{(1+z_1)} = 0.001$.

A summary of the aforementioned papers, along with the derived parameters, are presented in Table 3 and Figure 13.

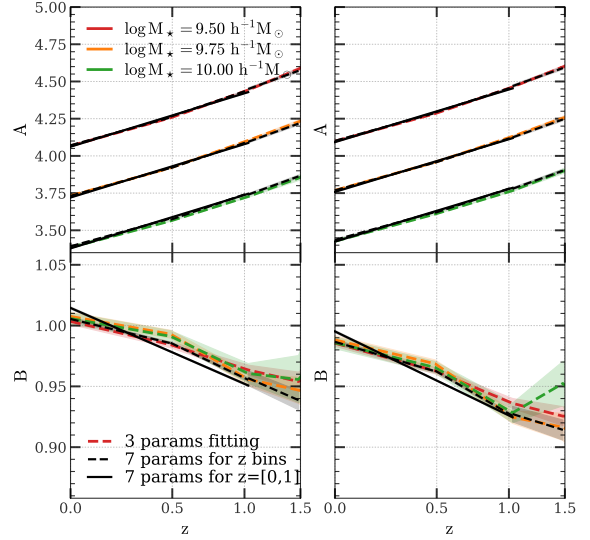


Figure 12. Similar to Figure 11, but for GIZMO-SIMBA. Scatter parameters have been omitted either.

Our comparison results start with an absolute magnitude threshold $\mathcal{M}_i = -19.47$ at $z = 0$, corresponding to 0.2 times the characteristic luminosity $0.2L_*$ applied in the redMaPPer algorithm (Rykoff et al. 2012, 2014). The threshold varies with redshift due to the passive evolution of the stellar population. To calculate the evolution and determine the threshold at the pivot redshift z_p , we utilize the FSPS code. More specifically, in the evolution model, we assume that the stellar population was formed at a redshift of $z_f = 3$, and adopt the 'MIST' stellar isochrone libraries (Choi et al. 2016), the 'MILES' stellar spectral libraries (Vazdekis et al. 2010), the IMF of Chabrier (2003) and the Solar metallicity. Ultimately, we obtain the threshold at z_p as $\mathcal{M}_i = -19.98$.

Next, we employ Equation (4) to obtain M_* , which is $4.77 \times 10^9 h^{-1} M_\odot$ for GADGET-X, and $6.70 \times 10^9 h^{-1} M_\odot$ for GIZMO-SIMBA. Subsequently, by applying 7-parameters fitting results based on a log-normal distribution at redshifts $z = [0, 1]$, the upper panel and the first column from Table 1 and Table 2, we obtain the MR relation. The first two rows of Table 3 present this relation in the form of $\{\lambda_p, B_p, C_p\}$ using Equation (7) for convenient comparison with others papers. Note that the scatter here is the result of multiplying by 1.5, which is due to the transition from threshold M_* to \mathcal{M}_i in Section 4.2.

Furthermore, it is important to note that the cluster finders used in the referenced papers only identify red-sequence galaxies, whereas our analysis does not distinguish between red and blue galaxies. So we incorporate the red sequence fraction f_{RS} Equation (13) from Hen-

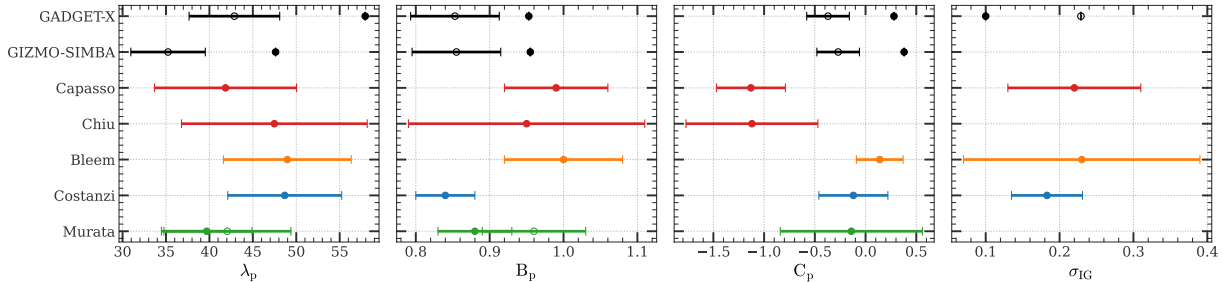


Figure 13. Parameters listed in Table 3. Colored dots represent parameters derived from the literature. Black dots show our results for full galaxies. Gray hollow dots indicate that the red fraction from Hennig et al. (2017) is taken into account. Green hollow dots represent results in the middle redshift range in Table 3 of Murata et al. (2019).

nig et al. (2017) :

$$f_{RS}(M, z) = A_{RS} \left(\frac{M}{6 \times 10^{14} M_{\odot}} \right)^{B_{RS}} \left(\frac{1+z}{1+0.46} \right)^{C_{RS}}. \quad (8)$$

Using the galaxy population of 74 SZ effect selected clusters from the SPT survey, Hennig et al. (2017) obtain $A_{RS} = 0.68 \pm 0.03$, $B_{RS} = -0.10 \pm 0.06$ and $C_{RS} = -0.65 \pm 0.21$. Converting this relation from their pivot point ($M = 6 \times 10^{14} M_{\odot}$, $z = 0.46$) to our pivot point ($M_p = 3 \times 10^{14} h^{-1} M_{\odot}$, $z_p = 0.5$) only affects the normalization parameter, resulting in $A_{RS} = 0.74 \pm 0.09$. Finally, the richness with red galaxies is represented as $\ln \lambda^{\text{red}} = \ln \lambda + \ln f_{RS}$, and the corresponding parameters $\{\lambda_p, B_p, C_p\}$ are shown in rows 3,4 of Table 3.

Each survey has its own strategy, so variations in λ_p are tolerable. Additionally, although most of them utilize redMaPPer as the cluster finder, the choice of filter bands differs, which can also impact the results.

Turning to B_p , Hennig et al. (2017) shows a decreasing mass trend of f_{RS} . But regardless of the inclusion of blue galaxies, mass trends of the MR relations are consistent in their work. In contrast, Okabe et al. (2019) illustrates a weakly increasing mass dependence of f_{RS} in their Figure 5. Our B_p values for full galaxies (black dots in Figure 13) demonstrate better consistency with the ICM-selected samples (red and orange dots). The other two optical-selected samples (blue and green dots) yield consistent results that are slightly smaller than ours. This divergence may be attributed to projection effects, which the ICM-selected cluster sample is not susceptible to. Murata et al. (2019) states that their results in the middle redshift range $z = [0.4, 0.7]$ are least affected by projection effects in Table 3. Specifically, they report a slope of $0.96^{+0.09}_{-0.07}$ for M_{200c} (green hollow dots in Figure 13), which helps mitigate inconsistencies.

Now turning to C_p , while most observations tend to indicate a negative C_p , our results show positive values (black dots). However, after accounting for f_{RS} , these values turn out to be negative (gray dots) and

exhibit more consistency with optical-selected samples (blue and green dots).

Finally, shifting our focus to scatter, previous studies by Capasso et al. (2019), Costanzi et al. (2021) and Bleem et al. (2020) have modeled scatter using the same form as Equation (3), albeit without considering the redshift dependence. Nevertheless, their values of σ_{IG} align with each other. When accounting for the red fraction $\sigma_{f_{RS}} = 0.14$, our σ_{IG} increases from 0.10 to 0.23. Furthermore, it is important to consider additional sources of scatter in observations, such as miscentering and projection effects (Rozo et al. 2011). Additionally, the choice of richness estimation methods employed by different cluster finders can also impact the scatter (Rykoff et al. 2012; Euclid Collaboration et al. 2019).

6. CONCLUSIONS

In this paper, we constrain the mass-richness (MR) relation of galaxy clusters with stellar mass-selected and magnitude-selected galaxies from two different hydrodynamic simulations, GADGET-X and GIZMO-SIMBA, from THE300 project. We model the distribution of richness at a fixed cluster mass by a skewed Gaussian distribution (Equation (2)) with a power-law scaling relation for the mean (Equation (1)). Our main results are as follows:

- We display the fitting parameters and their variations with respect to the stellar mass threshold M_{\star} and redshift z in Figure 7. The variation depends strongly on the baryon models when $M_{\star} \gtrsim 10^{10} h^{-1} M_{\odot}$. However, it is more stable with a lower M_{\star} . For lower M_{\star} , the amplitude A decreases with M_{\star} , increases with z , and these dependencies are independent. The slope B and the scatter σ_{I} remain constant with M_{\star} , while B decreases with z and σ_{I} exhibits the opposite trend.
- We compare the fitting results from GADGET-X and GIZMO-SIMBA in Figure 7. For lower M_{\star} , GIZMO-SIMBA displays a stronger redshift

Table 3. Richness–mass–redshift relation parameters from this analysis and the literature. λ_p is richness at the pivot point $M_p = 3 \times 10^{14} h^{-1} M_\odot$, $z_p = 0.5$. B_p and C_p denote the mass and redshift dependencies, respectively, around the pivot point.

Simulations	$M_\star [h^{-1} M_\odot]$ at z_p	λ_p	M^{B_p}	$(1+z)^{C_p}$	σ_{IG}
GADGET-X	4.77×10^9	57.94	0.953	0.28	0.10
GIZMO-SIMBA	6.70×10^9	47.62	0.955	0.38	/
Red galaxies	$\ln f_{RS} = \ln(0.74 \pm 0.09) - (0.10 \pm 0.06) \ln \frac{M}{M_p} - (0.65 \pm 0.21) \ln \frac{1+z}{1+z_p}$				
GADGET-X	4.77×10^9	42.88 ± 5.21	0.853 ± 0.06	-0.37 ± 0.21	0.23
GIZMO-SIMBA	6.70×10^9	35.24 ± 4.29	0.855 ± 0.06	-0.27 ± 0.21	/
Authors	Description	λ_p	M^{B_p}	$(1+z)^{C_p}$	σ_{IG}
Capasso et al. (2019)	ROSAT galaxy dynamics	$41.85^{+7.98}_{-8.18}$	$0.99^{+0.06}_{-0.07}$	$-1.13^{+0.32}_{-0.34}$	$0.22^{+0.08}_{-0.09}$
Murata et al. (2019)	HSC NC	$39.69^{+5.71}_{-5.22}$	$0.88^{+0.05}_{-0.05}$	$-0.14^{+0.59}_{-0.70}$	/
Bleem et al. (2020)	SPT NC	$48.97^{+8.01}_{-7.36}$	$1.00^{+0.08}_{-0.08}$	$0.14^{+0.23}_{-0.23}$	$0.23^{+0.16}_{-0.16}$
Costanzi et al. (2021)	DES NC + SPT OMR	$48.67^{+5.55}_{-6.56}$	$0.84^{+0.04}_{-0.04}$	$-0.12^{+0.34}_{-0.34}$	$0.207^{+0.061}_{-0.045}$
Chiu et al. (2023)	eROSITA NC	$47.48^{+11.67}_{-10.69}$	$0.95^{+0.17}_{-0.16}$	$-1.12^{+0.54}_{-0.65}$	/

evolution for A and a negligible σ_{I} . The slope B is consistent for the two simulations.

- We present the fitting parameters obtained from stellar mass-selected and magnitude-selected galaxies in Figure 10. The relative difference in $\{A, B\}$ is within 5%. However, σ_{I} increases by 50% in the magnitude-selected case. The relative difference between GADGET-X and GIZMO-SIMBA is basically propagated from M_\star limit to magnitude limit.
- Additionally, we compare our skewed Gaussian distribution for the richness with the widely used log-normal distribution with a scatter given by Equation (B1), as depicted in Figure 16, or a scatter σ_{IG} given by Equation (3), as depicted in Figure 4. The former exhibits a more intricate scatter with coupled and non-linear dependencies on halo mass, galaxy stellar mass threshold and redshift, while the latter demonstrates a mass dependence in σ_{IG} , which has been overlooked in previous work.
- We provide the results of a 7-parameter fitting incorporating dependence on galaxy selection threshold and redshift for both the skewed Gaussian and log-normal distributions in Table 1 and Table 2.
- Finally, to compare our findings with observational results in the literature, we combine our 7-parameter MR relation with the stellar mass-magnitude relation (Equation (4)). The results are shown in Figure 13. After considering the red fraction, our results are consistent with the majority of literature at a pivot point, regarding rich-

ness, mass dependence, redshift dependence, and scatter.

Based on these results, we have established the MR relations from hydrodynamic simulations and demonstrated their applicability to actual observations. The differences between GADGET-X and GIZMO-SIMBA simulations offer valuable insights into the evolution of galaxies. While considering secondary halo properties, such as age and concentration, is expected to decrease the scatter in this relation (Hearin et al. 2013; Bradshaw et al. 2020; Farahi et al. 2020), it is important to note that the intrinsic scatter σ_{I} defined in this paper is more likely to originate from the large-scale environment with a strong dependence on baryon models. Further research and investigation (in preparation) are required to better understand the underlying physics.

One limitation of this study is the incompleteness of the low halo mass sample, especially at high redshifts, which can introduce biases to the result from the environmental effect. This is because the low-mass halos in THE300 regions are mainly surrounded by the central clusters, which may cause some differences from those in other environments. However, we think the effect should be very small (Wang et al. 2018), especially for the galaxy number count with a large stellar mass cut.

Recently, there has been a lot of work using machine learning to estimate the mass of individual clusters (e.g. Ntampaka et al. 2015, 2019; Yan et al. 2020; Ferragamo et al. 2023; de Andres et al. 2023). This data-driven approach circumvents the need for dynamical or hydrostatic assumptions, effectively reducing the bias. Concurrently, numerous new mass proxies have emerged, including stellar mass (e.g. Andreon 2012; Kravtsov et al. 2018; Pereira et al. 2020; Bradshaw et al. 2020), stellar density profile (e.g. Huang et al. 2022) and intra-cluster

light profile (e.g. Montes & Trujillo 2019; Alonso Asensio et al. 2020, and Contreras-Santos et al. in prep.). Combining these studies, we expect that enhanced accuracy will be achieved in cluster cosmology and deeper comprehension will be brought to the formation and evolution of galaxies.

1 This work is supported by the National Key R&D
 2 Program of China Grant No. 2022YFF0503404 and
 3 No. 2021YFC2203100, by the National Natural Sci-
 4 ence Foundation of China Grants No. 12173036 and
 5 11773024, by the China Manned Space Project “Prob-
 6 ing dark energy, modified gravity and cosmic struc-
 7 ture formation by CSST multi-cosmological measure-
 8 ments” and Grant No. CMS-CSST-2021-B01, by the
 9 Fundamental Research Funds for Central Universities
 10 Grants No. WK3440000004 and WK3440000005, by
 11 Cyrus Chun Ying Tang Foundations, and by the 111
 12 Project for “Observational and Theoretical Research on
 13 Dark Matter and Dark Energy” (B23042). WC is also
 14 supported by the STFC AGP Grant ST/V000594/1,
 15 and the Atracción de Talento Contract no. 2020-
 16 T1/TIC-19882 granted by the Comunidad de Madrid in
 17 Spain. He also thanks the Ministerio de Ciencia e Inno-
 18 vación (Spain) for financial support under Project grant
 19 PID2021-122603NB-C21 and ERC: HORIZON-TMA-
 20 MSCA-SE for supporting the LACEGAL-III project
 21 with grant number 101086388.

22 The simulations were performed at the MareNos-
 23 trum Supercomputer of the BSC-CNS through The Red
 24 Española de Supercomputación grants (AECT-2022-3-
 25 0027, AECT-2023-1-0013), and at the DiAL – DiRAC
 26 machines at the University of Leicester through the
 27 RAC15 grant: Seedcorn/ACTP317

APPENDIX

A. RICHNESS PROBABILITY DISTRIBUTIONS

This section serves as a supplement to Section 3.1.

In Figure 14, we show examples utilizing the skewed Gaussian function and the log-normal function to fit the individual richness probability distributions from both GADGET-X and GIZMO-SIMBA data in two mass bins at $z = 0$. Both galaxy selections, i.e. the stellar mass M_* and magnitude \mathcal{M}_i , have been considered. The former function demonstrates better incorporation of low richness values, and both functions exhibit greater consistency in the larger mass bin.

Additionally, we compute the ratio of residuals obtained from the skewed Gaussian function and the log-normal function. As illustrated in Figure 15, this ratio is largely less than 1, especially in the low mass bin.

B. ANOTHER FORM FOR THE SCATTER

There is another widely used assumption for the richness probability distribution (Murata et al. 2018, 2019), a log-normal form with a scatter that varies linearly with mass:

$$\sigma_{\ln \lambda} = \sigma_0 + q \ln \left(\frac{M}{M_{piv}} \right), \quad (\text{B1})$$

involving more parameters than ours. Nevertheless, we still repeat the procedure described in Section 4.1 to estimate the four parameters $\{A, B, \sigma_0, q\}$ for comparison. As depicted in Figure 16, the parameters $\{A, B\}$ are slightly different from our results, while the scatter σ_0 , in particular, shows a strong dependence on M_* .

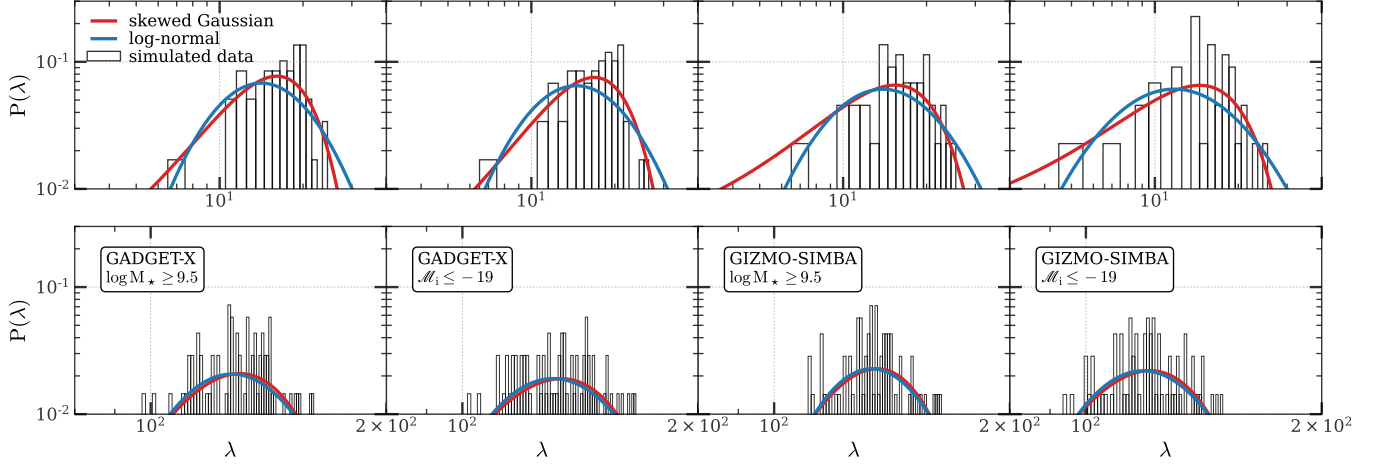


Figure 14. Similar to Figure 3. Upper and lower panels correspond to mass bin $\log M[h^{-1}M_{\odot}] = [13.90, 13.95]$ and $\log M[h^{-1}M_{\odot}] = [14.80, 14.85]$, respectively. Each column represents different simulations, GADGET-X or GIZMO-SIMBA, as well as different galaxy selection thresholds, $\log M_{\star}[h^{-1}M_{\odot}] \geq 9.5$ or $\mathcal{M}_i \leq -19$, as labeled in the legend.

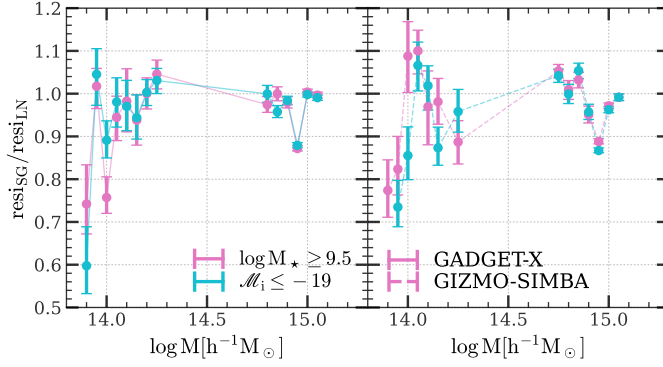


Figure 15. The ratio between residual using the skewed Gaussian function(res_{IG}) and residual using the log-normal function(res_{LN}). The left(solid lines) and right(dashed lines) panels correspond to GADGET-X and GIZMO-SIMBA respectively. Different colors represent different galaxy selection thresholds, $\log M_{\star}[h^{-1}M_{\odot}] \geq 9.5$ (pink) or $\mathcal{M}_i \leq -19$ (cyan).

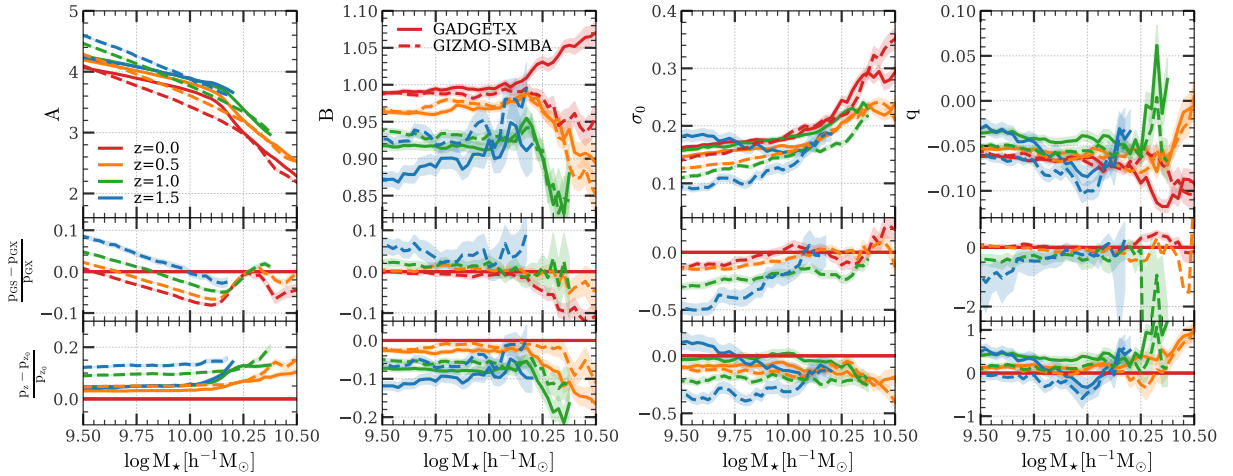


Figure 16. Similar to Figure 7, but for parameters $\{A, B, \sigma_0, q\}$.

C. DIFFERENT BANDS

We fit the galaxy stellar mass-absolute magnitude $M_\star - \mathcal{M}$ relation in CSST-z band \mathcal{M}_z and Euclid-h band \mathcal{M}_h for both GADGET-X and GIZMO-SIMBA. The comparison results of the parameters are shown in Figure 17 and Figure 18.

GADGET-X:

$$\begin{aligned} \ln M_\star &= 4.57 - 0.90 \mathcal{M}_z - 1.20 \times \ln(1+z), \\ \ln M_\star &= 4.68 - 0.88 \mathcal{M}_h - 1.00 \times \ln(1+z). \end{aligned} \quad (\text{C2})$$

GIZMO-SIMBA:

$$\begin{aligned} \ln M_\star &= 4.23 - 0.92 \mathcal{M}_z - 1.00 \times \ln(1+z), \\ \ln M_\star &= 4.09 - 0.91 \mathcal{M}_h - 0.89 \times \ln(1+z). \end{aligned} \quad (\text{C3})$$

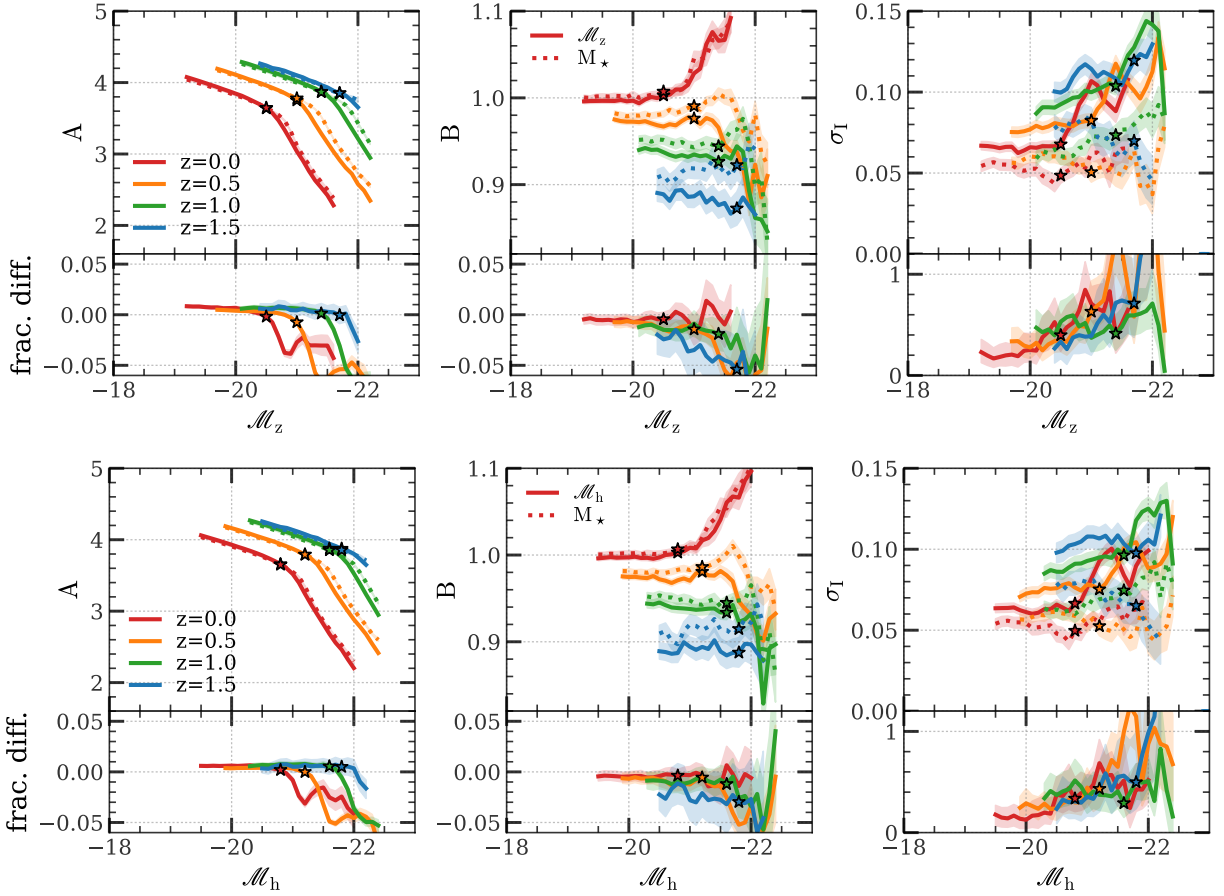


Figure 17. Similar to Figure 10. The upper panel is in CSST z-band. The lower panel is in Euclid h-band.

D. APPLICATION IN CSST

We give an example employing the apparent magnitude threshold $m_i = 25.9$ from Gong et al. (2019) to derive the MR relation. We use a simple relation, without K-correction or evolutionary correction,

$$\mathcal{M}_i = m_i - 5 \log \frac{D_L}{10 \text{pc}}, \quad (\text{D4})$$

to convert the apparent magnitude m_i to the absolute magnitude \mathcal{M}_i at redshift $z = \{0, 1, 1.5\}$. Equation (4) is then utilized to obtain M_\star . Next, by applying 7-parameters fitting results based on a log-normal distribution at each

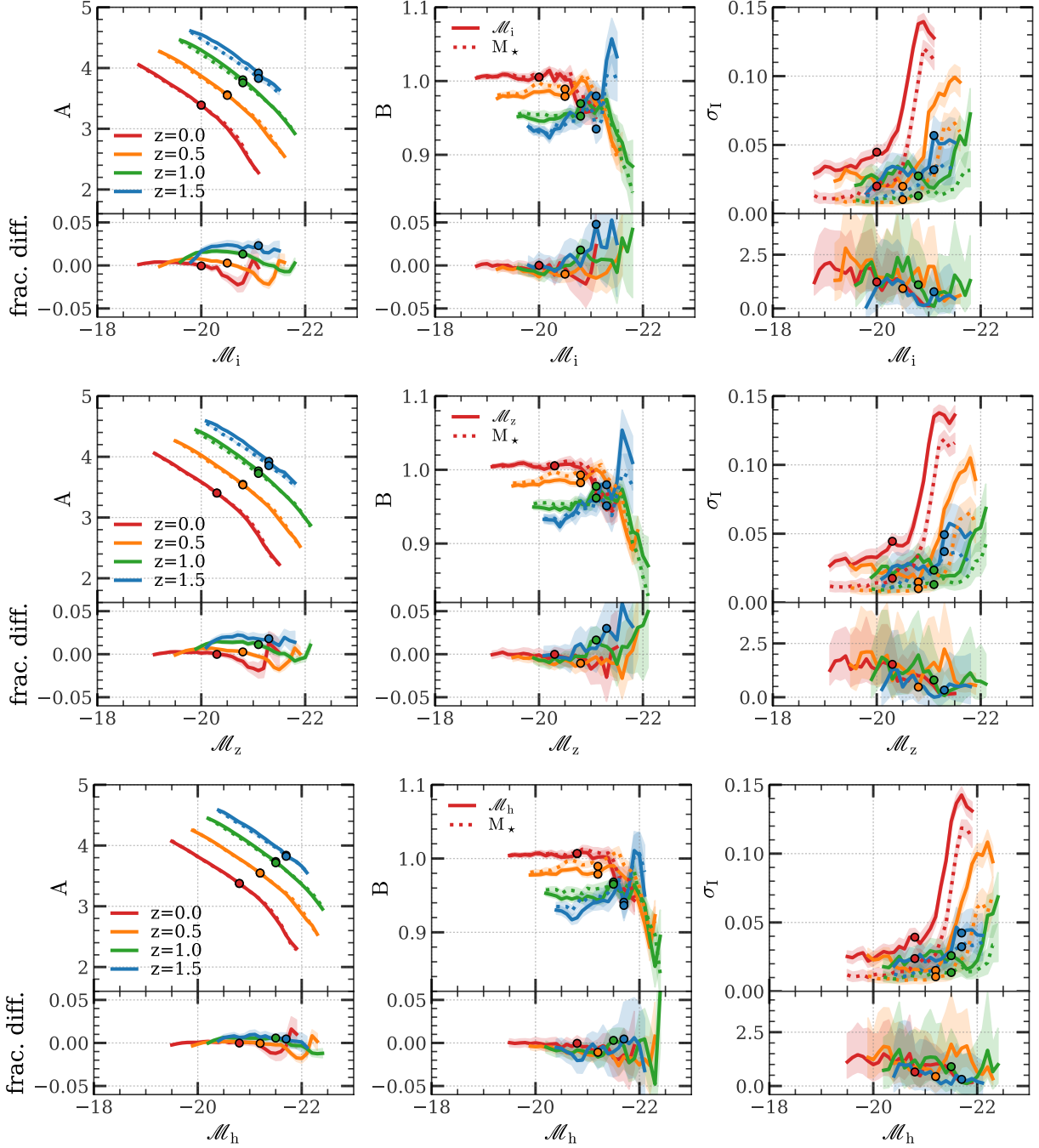


Figure 18. Similar to Figure 10, but for GIZMO-SIMBA. The upper panel is in CSST i-band. The middle panel is in CSST z-band. The lower panel is in Euclid h-band.

redshift bin $z = [0, 0.5], [0.5, 1], [1, 1.5]$ from Table 1 and Table 2, we obtain the MR relation displayed as 3 parameters, as Table 4 shows. Note that the scatter here is the result of multiplying by 1.5, which is due to the transition from threshold M_* to \mathcal{M} in Section 4.2. We would like to emphasize that this is merely an illustrative example and the threshold should be determined based on different cluster finders and richness estimators when practically applied, as demonstrated in Section 5.3.

REFERENCES

Table 4. Derived 3-parameters at the threshold $m_i = 25.9$. $\{A, B, \sigma_I\}$ represents the skewed Gaussian distribution. $\{A, B, \sigma_{IG}\}$ represents the log-normal distribution.

z	\mathcal{M}_i	$M_* [h^{-1}M_\odot]$	A	B	σ_I	A	B	σ_{IG}
GADGET-X								
0.5	-16.39	1.82×10^8	5.093	0.980	0.088	5.096	0.958	0.094
1.0	-18.20	6.50×10^8	4.766	0.952	0.094	4.765	0.916	0.114
1.5	-19.27	1.29×10^9	4.535	0.910	0.116	4.534	0.881	0.131
GIZMO-SIMBA								
0.5	-16.39	2.38×10^8	5.825	0.985	-	5.810	0.962	-
1.0	-18.20	9.34×10^8	5.192	0.958	-	5.190	0.928	-
1.5	-19.27	1.98×10^9	4.865	0.938	-	4.875	0.914	-

- Ahad, S. L., Bahé, Y. M., Hoekstra, H., van der Burg, R. F. J., & Muzzin, A. 2021, MNRAS, 504, 1999, doi: [10.1093/mnras/stab1036](https://doi.org/10.1093/mnras/stab1036)
- Allen, S. W., Evrard, A. E., & Mantz, A. B. 2011, ARA&A, 49, 409, doi: [10.1146/annurev-astro-081710-102514](https://doi.org/10.1146/annurev-astro-081710-102514)
- Alonso Asensio, I., Dalla Vecchia, C., Bahé, Y. M., Barnes, D. J., & Kay, S. T. 2020, MNRAS, 494, 1859, doi: [10.1093/mnras/staa861](https://doi.org/10.1093/mnras/staa861)
- Anbajagane, D., Evrard, A. E., Farahi, A., et al. 2020, MNRAS, 495, 686, doi: [10.1093/mnras/staa1147](https://doi.org/10.1093/mnras/staa1147)
- Andreon, S. 2012, A&A, 548, A83, doi: [10.1051/0004-6361/201220284](https://doi.org/10.1051/0004-6361/201220284)
- Andreon, S., & Congdon, P. 2014, A&A, 568, A23, doi: [10.1051/0004-6361/201423616](https://doi.org/10.1051/0004-6361/201423616)
- Ansarifard, S., Rasia, E., Biffi, V., et al. 2020, A&A, 634, A113, doi: [10.1051/0004-6361/201936742](https://doi.org/10.1051/0004-6361/201936742)
- Arthur, J., Pearce, F. R., Gray, M. E., et al. 2019, MNRAS, 484, 3968, doi: [10.1093/mnras/stz212](https://doi.org/10.1093/mnras/stz212)
- Babik, I. V., & McNamara, B. R. 2023, ApJ, 946, 54, doi: [10.3847/1538-4357/acbf4b](https://doi.org/10.3847/1538-4357/acbf4b)
- Baxter, E. J., Adhikari, S., Vega-Ferrero, J., et al. 2021, MNRAS, 508, 1777, doi: [10.1093/mnras/stab2720](https://doi.org/10.1093/mnras/stab2720)
- Bernardi, M., Sheth, R. K., Fischer, J. L., et al. 2018, MNRAS, 475, 757, doi: [10.1093/mnras/stx3171](https://doi.org/10.1093/mnras/stx3171)
- Bleem, L. E., Bocquet, S., Stalder, B., et al. 2020, ApJS, 247, 25, doi: [10.3847/1538-4365/ab6993](https://doi.org/10.3847/1538-4365/ab6993)
- Bradshaw, C., Leauthaud, A., Hearin, A., Huang, S., & Behroozi, P. 2020, MNRAS, 493, 337, doi: [10.1093/mnras/staa081](https://doi.org/10.1093/mnras/staa081)
- Capalbo, V., De Petris, M., De Luca, F., et al. 2021, MNRAS, 503, 6155, doi: [10.1093/mnras/staa3900](https://doi.org/10.1093/mnras/staa3900)
- Capasso, R., Mohr, J. J., Saro, A., et al. 2019, MNRAS, 486, 1594, doi: [10.1093/mnras/stz931](https://doi.org/10.1093/mnras/stz931)
- Cappellari, M., McDermid, R. M., Alatalo, K., et al. 2012, Nature, 484, 485, doi: [10.1038/nature10972](https://doi.org/10.1038/nature10972)
- Chabrier, G. 2003, PASP, 115, 763, doi: [10.1086/376392](https://doi.org/10.1086/376392)
- Charlot, S., & Fall, S. M. 2000, ApJ, 539, 718, doi: [10.1086/309250](https://doi.org/10.1086/309250)
- Chiu, I. N., Klein, M., Mohr, J., & Bocquet, S. 2023, MNRAS, 522, 1601, doi: [10.1093/mnras/stad957](https://doi.org/10.1093/mnras/stad957)
- Choi, J., Dotter, A., Conroy, C., et al. 2016, ApJ, 823, 102, doi: [10.3847/0004-637X/823/2/102](https://doi.org/10.3847/0004-637X/823/2/102)
- Conroy, C., & Gunn, J. E. 2010, ApJ, 712, 833, doi: [10.1088/0004-637X/712/2/833](https://doi.org/10.1088/0004-637X/712/2/833)
- Conroy, C., Gunn, J. E., & White, M. 2009, ApJ, 699, 486, doi: [10.1088/0004-637X/699/1/486](https://doi.org/10.1088/0004-637X/699/1/486)
- Contreras, S., & Zehavi, I. 2023, MNRAS, 525, 4257, doi: [10.1093/mnras/stad2452](https://doi.org/10.1093/mnras/stad2452)
- Contreras, S., Zehavi, I., Baugh, C. M., Padilla, N., & Norberg, P. 2017, MNRAS, 465, 2833, doi: [10.1093/mnras/stw2826](https://doi.org/10.1093/mnras/stw2826)
- Costanzi, M., Rozo, E., Simet, M., et al. 2019, MNRAS, 488, 4779, doi: [10.1093/mnras/stz1949](https://doi.org/10.1093/mnras/stz1949)
- Costanzi, M., Saro, A., Bocquet, S., et al. 2021, PhRvD, 103, 043522, doi: [10.1103/PhysRevD.103.043522](https://doi.org/10.1103/PhysRevD.103.043522)
- Cui, W., Knebe, A., Yepes, G., et al. 2018, MNRAS, 480, 2898, doi: [10.1093/mnras/sty2111](https://doi.org/10.1093/mnras/sty2111)
- Cui, W., Dave, R., Knebe, A., et al. 2022, MNRAS, 514, 977, doi: [10.1093/mnras/stac1402](https://doi.org/10.1093/mnras/stac1402)
- Davé, R., Anglés-Alcázar, D., Narayanan, D., et al. 2019, MNRAS, 486, 2827, doi: [10.1093/mnras/stz937](https://doi.org/10.1093/mnras/stz937)
- de Andres, D., Cui, W., Yepes, G., et al. 2023, arXiv e-prints, arXiv:2311.02469, doi: [10.48550/arXiv.2311.02469](https://doi.org/10.48550/arXiv.2311.02469)
- de Andres, D., Cui, W., Ruppin, F., et al. 2022, Nature Astronomy, 6, 1325, doi: [10.1038/s41550-022-01784-y](https://doi.org/10.1038/s41550-022-01784-y)
- De Luca, F., De Petris, M., Yepes, G., et al. 2021, MNRAS, 504, 5383, doi: [10.1093/mnras/stab1073](https://doi.org/10.1093/mnras/stab1073)

- Duffy, A. R., Schaye, J., Kay, S. T., & Dalla Vecchia, C. 2008, *MNRAS*, 390, L64, doi: [10.1111/j.1745-3933.2008.00537.x](https://doi.org/10.1111/j.1745-3933.2008.00537.x)
- Euclid Collaboration, Adam, R., Vannier, M., et al. 2019, *A&A*, 627, A23, doi: [10.1051/0004-6361/201935088](https://doi.org/10.1051/0004-6361/201935088)
- Euclid Collaboration, Giocoli, C., Meneghetti, M., et al. 2023, arXiv e-prints, arXiv:2302.00687, doi: [10.48550/arXiv.2302.00687](https://doi.org/10.48550/arXiv.2302.00687)
- Evrard, A. E., Arnault, P., Huterer, D., & Farahi, A. 2014, *MNRAS*, 441, 3562, doi: [10.1093/mnras/stu784](https://doi.org/10.1093/mnras/stu784)
- Farahi, A., Ho, M., & Trac, H. 2020, *MNRAS*, 493, 1361, doi: [10.1093/mnras/staa291](https://doi.org/10.1093/mnras/staa291)
- Ferragamo, A., de Andres, D., Sbriglio, A., et al. 2023, *MNRAS*, 520, 4000, doi: [10.1093/mnras/stad377](https://doi.org/10.1093/mnras/stad377)
- Foreman-Mackey, D., Hogg, D. W., Lang, D., & Goodman, J. 2013, *PASP*, 125, 306, doi: [10.1086/670067](https://doi.org/10.1086/670067)
- Gianfagna, G., Rasia, E., Cui, W., et al. 2023, *MNRAS*, 518, 4238, doi: [10.1093/mnras/stac3364](https://doi.org/10.1093/mnras/stac3364)
- Gianfagna, G., De Petris, M., Yepes, G., et al. 2021, *MNRAS*, 502, 5115, doi: [10.1093/mnras/stab308](https://doi.org/10.1093/mnras/stab308)
- Gong, Y., Liu, X., Cao, Y., et al. 2019, *ApJ*, 883, 203, doi: [10.3847/1538-4357/ab391e](https://doi.org/10.3847/1538-4357/ab391e)
- Gunawardhana, M. L. P., Hopkins, A. M., Sharp, R. G., et al. 2011, *MNRAS*, 415, 1647, doi: [10.1111/j.1365-2966.2011.18800.x](https://doi.org/10.1111/j.1365-2966.2011.18800.x)
- Haggar, R., Gray, M. E., Pearce, F. R., et al. 2020, *MNRAS*, 492, 6074, doi: [10.1093/mnras/staa273](https://doi.org/10.1093/mnras/staa273)
- Hearin, A. P., Zentner, A. R., Newman, J. A., & Berlind, A. A. 2013, *MNRAS*, 430, 1238, doi: [10.1093/mnras/sts699](https://doi.org/10.1093/mnras/sts699)
- Hennig, C., Mohr, J. J., Zenteno, A., et al. 2017, *MNRAS*, 467, 4015, doi: [10.1093/mnras/stx175](https://doi.org/10.1093/mnras/stx175)
- Herbonnet, R., Crawford, A., Avestruz, C., et al. 2022, *MNRAS*, 513, 2178, doi: [10.1093/mnras/stac997](https://doi.org/10.1093/mnras/stac997)
- Huang, S., Leauthaud, A., Bradshaw, C., et al. 2022, *MNRAS*, 515, 4722, doi: [10.1093/mnras/stac1680](https://doi.org/10.1093/mnras/stac1680)
- Jiang, F., & van den Bosch, F. C. 2017, *MNRAS*, 472, 657, doi: [10.1093/mnras/stx1979](https://doi.org/10.1093/mnras/stx1979)
- Jiménez Muñoz, A., Macías-Pérez, J. F., Yepes, G., et al. 2023, arXiv e-prints, arXiv:2309.01443, doi: [10.48550/arXiv.2309.01443](https://doi.org/10.48550/arXiv.2309.01443)
- Kaiser, N. 1986, *MNRAS*, 222, 323, doi: [10.1093/mnras/222.2.323](https://doi.org/10.1093/mnras/222.2.323)
- Klypin, A., Yepes, G., Gottlöber, S., Prada, F., & Heß, S. 2016, *MNRAS*, 457, 4340, doi: [10.1093/mnras/stw248](https://doi.org/10.1093/mnras/stw248)
- Knebe, A., Gámez-Marín, M., Pearce, F. R., et al. 2020, *MNRAS*, 495, 3002, doi: [10.1093/mnras/staa1407](https://doi.org/10.1093/mnras/staa1407)
- Knollmann, S. R., & Knebe, A. 2009, *ApJS*, 182, 608, doi: [10.1088/0067-0049/182/2/608](https://doi.org/10.1088/0067-0049/182/2/608)
- Kravtsov, A. V., Berlind, A. A., Wechsler, R. H., et al. 2004, *ApJ*, 609, 35, doi: [10.1086/420959](https://doi.org/10.1086/420959)
- Kravtsov, A. V., & Borgani, S. 2012, *ARA&A*, 50, 353, doi: [10.1146/annurev-astro-081811-125502](https://doi.org/10.1146/annurev-astro-081811-125502)
- Kravtsov, A. V., Vikhlinin, A. A., & Meshcheryakov, A. V. 2018, *Astronomy Letters*, 44, 8, doi: [10.1134/S1063773717120015](https://doi.org/10.1134/S1063773717120015)
- Kuchner, U., Aragón-Salamanca, A., Pearce, F. R., et al. 2020, *MNRAS*, 494, 5473, doi: [10.1093/mnras/staa1083](https://doi.org/10.1093/mnras/staa1083)
- Kuchner, U., Aragón-Salamanca, A., Rost, A., et al. 2021, *MNRAS*, 503, 2065, doi: [10.1093/mnras/stab567](https://doi.org/10.1093/mnras/stab567)
- Laureijs, R., Amiaux, J., Arduini, S., et al. 2011, arXiv e-prints, arXiv:1110.3193, doi: [10.48550/arXiv.1110.3193](https://doi.org/10.48550/arXiv.1110.3193)
- Lewis, A. D., Ellingson, E., Morris, S. L., & Carlberg, R. G. 1999, *ApJ*, 517, 587, doi: [10.1086/307204](https://doi.org/10.1086/307204)
- Li, Q., Han, J., Wang, W., et al. 2022, *MNRAS*, 514, 5890, doi: [10.1093/mnras/stac1739](https://doi.org/10.1093/mnras/stac1739)
- . 2021, *MNRAS*, 505, 3907, doi: [10.1093/mnras/stab1633](https://doi.org/10.1093/mnras/stab1633)
- Li, Q., Narayanan, D., & Davé, R. 2019, *MNRAS*, 490, 1425, doi: [10.1093/mnras/stz2684](https://doi.org/10.1093/mnras/stz2684)
- Li, Q., Cui, W., Yang, X., et al. 2020, *MNRAS*, 495, 2930, doi: [10.1093/mnras/staa1385](https://doi.org/10.1093/mnras/staa1385)
- . 2023, *MNRAS*, 523, 1228, doi: [10.1093/mnras/stad1521](https://doi.org/10.1093/mnras/stad1521)
- Mao, Y.-Y., Williamson, M., & Wechsler, R. H. 2015, *ApJ*, 810, 21, doi: [10.1088/0004-637X/810/1/21](https://doi.org/10.1088/0004-637X/810/1/21)
- McClintock, T., Varga, T. N., Gruen, D., et al. 2019, *MNRAS*, 482, 1352, doi: [10.1093/mnras/sty2711](https://doi.org/10.1093/mnras/sty2711)
- Meneghetti, M., Fedeli, C., Pace, F., Gottlöber, S., & Yepes, G. 2010, *A&A*, 519, A90, doi: [10.1051/0004-6361/201014098](https://doi.org/10.1051/0004-6361/201014098)
- Montes, M., & Trujillo, I. 2019, *MNRAS*, 482, 2838, doi: [10.1093/mnras/sty2858](https://doi.org/10.1093/mnras/sty2858)
- Mostoghiu, R., Knebe, A., Cui, W., et al. 2019, *MNRAS*, 483, 3390, doi: [10.1093/mnras/sty3306](https://doi.org/10.1093/mnras/sty3306)
- Mulroy, S. L., Farahi, A., Evrard, A. E., et al. 2019, *MNRAS*, 484, 60, doi: [10.1093/mnras/sty3484](https://doi.org/10.1093/mnras/sty3484)
- Murata, R., Nishimichi, T., Takada, M., et al. 2018, *ApJ*, 854, 120, doi: [10.3847/1538-4357/aaaab8](https://doi.org/10.3847/1538-4357/aaaab8)
- Murata, R., Oguri, M., Nishimichi, T., et al. 2019, *PASJ*, 71, 107, doi: [10.1093/pasj/psz092](https://doi.org/10.1093/pasj/psz092)
- Narayanan, D., & Davé, R. 2012, *MNRAS*, 423, 3601, doi: [10.1111/j.1365-2966.2012.21159.x](https://doi.org/10.1111/j.1365-2966.2012.21159.x)
- Navarro, J. F., Frenk, C. S., & White, S. D. M. 1997, *ApJ*, 490, 493, doi: [10.1086/304888](https://doi.org/10.1086/304888)
- Ntampaka, M., Trac, H., Sutherland, D. J., et al. 2015, *ApJ*, 803, 50, doi: [10.1088/0004-637X/803/2/50](https://doi.org/10.1088/0004-637X/803/2/50)
- Ntampaka, M., ZuHone, J., Eisenstein, D., et al. 2019, *ApJ*, 876, 82, doi: [10.3847/1538-4357/ab14eb](https://doi.org/10.3847/1538-4357/ab14eb)
- Oguri, M., & Takada, M. 2011, *PhRvD*, 83, 023008, doi: [10.1103/PhysRevD.83.023008](https://doi.org/10.1103/PhysRevD.83.023008)

- Okabe, N., & Smith, G. P. 2016, *MNRAS*, 461, 3794, doi: [10.1093/mnras/stw1539](https://doi.org/10.1093/mnras/stw1539)
- Okabe, N., Oguri, M., Akamatsu, H., et al. 2019, *PASJ*, 71, 79, doi: [10.1093/pasj/psz059](https://doi.org/10.1093/pasj/psz059)
- Old, L., Skibba, R. A., Pearce, F. R., et al. 2014, *MNRAS*, 441, 1513, doi: [10.1093/mnras/stu545](https://doi.org/10.1093/mnras/stu545)
- Old, L., Wojtak, R., Mamon, G. A., et al. 2015, *MNRAS*, 449, 1897, doi: [10.1093/mnras/stv421](https://doi.org/10.1093/mnras/stv421)
- Pearce, F. A., Kay, S. T., Barnes, D. J., Bower, R. G., & Schaller, M. 2020, *MNRAS*, 491, 1622, doi: [10.1093/mnras/stz3003](https://doi.org/10.1093/mnras/stz3003)
- Pearson, R. J., Ponman, T. J., Norberg, P., Robotham, A. S. G., & Farr, W. M. 2015, *MNRAS*, 449, 3082, doi: [10.1093/mnras/stv463](https://doi.org/10.1093/mnras/stv463)
- Pereira, M. E. S., Palmese, A., Varga, T. N., et al. 2020, *MNRAS*, 498, 5450, doi: [10.1093/mnras/staa2687](https://doi.org/10.1093/mnras/staa2687)
- Planck Collaboration, Ade, P. A. R., Aghanim, N., et al. 2016a, *A&A*, 594, A24, doi: [10.1051/0004-6361/201525833](https://doi.org/10.1051/0004-6361/201525833)
- . 2016b, *A&A*, 594, A13, doi: [10.1051/0004-6361/201525830](https://doi.org/10.1051/0004-6361/201525830)
- Pratt, G. W., Arnaud, M., Biviano, A., et al. 2019, *SSRv*, 215, 25, doi: [10.1007/s11214-019-0591-0](https://doi.org/10.1007/s11214-019-0591-0)
- Rasia, E., Borgani, S., Murante, G., et al. 2015, *ApJL*, 813, L17, doi: [10.1088/2041-8205/813/1/L17](https://doi.org/10.1088/2041-8205/813/1/L17)
- Rost, A., Kuchner, U., Welker, C., et al. 2021, *MNRAS*, 502, 714, doi: [10.1093/mnras/staa3792](https://doi.org/10.1093/mnras/staa3792)
- Rost, A. M., Nuza, S. E., Stasyszyn, F., et al. 2024, *MNRAS*, 527, 1301, doi: [10.1093/mnras/stad3208](https://doi.org/10.1093/mnras/stad3208)
- Rozo, E., Rykoff, E., Koester, B., et al. 2011, *ApJ*, 740, 53, doi: [10.1088/0004-637X/740/2/53](https://doi.org/10.1088/0004-637X/740/2/53)
- Rykoff, E. S., Koester, B. P., Rozo, E., et al. 2012, *ApJ*, 746, 178, doi: [10.1088/0004-637X/746/2/178](https://doi.org/10.1088/0004-637X/746/2/178)
- Rykoff, E. S., Rozo, E., Busha, M. T., et al. 2014, *ApJ*, 785, 104, doi: [10.1088/0004-637X/785/2/104](https://doi.org/10.1088/0004-637X/785/2/104)
- Saro, A., Bocquet, S., Rozo, E., et al. 2015, *MNRAS*, 454, 2305, doi: [10.1093/mnras/stv2141](https://doi.org/10.1093/mnras/stv2141)
- Sembolini, F., Yepes, G., De Petris, M., et al. 2013, *MNRAS*, 429, 323, doi: [10.1093/mnras/sts339](https://doi.org/10.1093/mnras/sts339)
- Simet, M., McClintock, T., Mandelbaum, R., et al. 2017, *MNRAS*, 466, 3103, doi: [10.1093/mnras/stw3250](https://doi.org/10.1093/mnras/stw3250)
- Vazdekis, A., Sánchez-Blázquez, P., Falcón-Barroso, J., et al. 2010, *MNRAS*, 404, 1639, doi: [10.1111/j.1365-2966.2010.16407.x](https://doi.org/10.1111/j.1365-2966.2010.16407.x)
- Vega-Ferrero, J., Dana, J. M., Diego, J. M., et al. 2021, *MNRAS*, 500, 247, doi: [10.1093/mnras/staa3235](https://doi.org/10.1093/mnras/staa3235)
- Wang, Y., Pearce, F., Knebe, A., et al. 2018, *ApJ*, 868, 130, doi: [10.3847/1538-4357/aae52e](https://doi.org/10.3847/1538-4357/aae52e)
- Wechsler, R. H., & Tinker, J. L. 2018, *ARA&A*, 56, 435, doi: [10.1146/annurev-astro-081817-051756](https://doi.org/10.1146/annurev-astro-081817-051756)
- Wen, Z. L., & Han, J. L. 2021, *MNRAS*, 500, 1003, doi: [10.1093/mnras/staa3308](https://doi.org/10.1093/mnras/staa3308)
- Wen, Z. L., Han, J. L., & Liu, F. S. 2012, *ApJS*, 199, 34, doi: [10.1088/0067-0049/199/2/34](https://doi.org/10.1088/0067-0049/199/2/34)
- Wojtak, R., Old, L., Mamon, G. A., et al. 2018, *MNRAS*, 481, 324, doi: [10.1093/mnras/sty2257](https://doi.org/10.1093/mnras/sty2257)
- Xu, K., Jing, Y. P., & Gao, H. 2022, *ApJ*, 939, 104, doi: [10.3847/1538-4357/ac8f47](https://doi.org/10.3847/1538-4357/ac8f47)
- Yan, Z., Mead, A. J., Van Waerbeke, L., Hinshaw, G., & McCarthy, I. G. 2020, *MNRAS*, 499, 3445, doi: [10.1093/mnras/staa3030](https://doi.org/10.1093/mnras/staa3030)
- Yang, X., Zhang, Y., Wang, H., et al. 2018, *ApJ*, 860, 30, doi: [10.3847/1538-4357/aac2ce](https://doi.org/10.3847/1538-4357/aac2ce)
- Zhan, H. 2011, *Sci. Sin. Phys. Mech. Astron.*, 41, 1441, doi: [10.1360/132011-961](https://doi.org/10.1360/132011-961)
- Zhang, B., Cui, W., Wang, Y., Dave, R., & De Petris, M. 2022, *MNRAS*, 516, 26, doi: [10.1093/mnras/stac2171](https://doi.org/10.1093/mnras/stac2171)
- Zheng, Z., Berlind, A. A., Weinberg, D. H., et al. 2005, *ApJ*, 633, 791, doi: [10.1086/466510](https://doi.org/10.1086/466510)
- Zwicky, F. 1937, *ApJ*, 86, 217, doi: [10.1086/143864](https://doi.org/10.1086/143864)